TALLINN UNIVERSITY OF TECHNOLOGY
School of Science
Applied Physics

Enrico Di Lavore 202374YAFM

NUMERICAL ANALYSIS OF RAYLEIGH-BÈNARD CONVECTIVE SCALING LAWS AT HIGH PRANDTL NUMBER

Master Thesis

Host University Supervisor
Prof. Andreas Tilgner
Home University Supervisor
Prof. Jaan Kalda

Göttingen 2022

Author’s declaration of originality

I hereby certify that I am the sole author of this thesis. All the used materials, references to the literature and the work of others have been referred to. This thesis has not been presented for examination anywhere else.

Author: Enrico Di Lavore ....

(signature)

Date: Month Day, 2022

Abstract

We obtain Rayleigh-Bénard convective scaling laws for the dimensionless Nusselt and Reynolds numbers as functions of Prandtl, Ekman and Rayleigh numbers, for large Prandtl numbers in rotating and non rotating systems. We have used numerical simulations based on the Navier-Stokes equations.

We have obtained the results by mean of a Spectral Method program, NEK5000, over a set of 63 simulations, each for a combination of Prandtl, Ekman and Rayleigh numbers (3Pr $\times$ 3Ek $\times$ 7Ra).

Dimensionless numbers are important identifiers of the characteristics of the flow; indeed flows can be classified in groups which have some dimensionless numbers in common. We have found that there is a treshold Prandtl number value over which the Nusselt and Reynolds numbers do not depend on the Prandtl number. In particular, the differences between the cases with Pr $= 100$, Pr $= 300$ and Pr $= \infty$ have been proved to be negligible. This is an important finding because the case Pr $= \infty$ corresponds to Steady Stokes flow by which viscosity dominates over inertial terms in the Navier-Stokes equation owing to which the computations are simplified and accelerated significantly.

Additionally, we have investigated the effect of rotation on convective motion onset. It has been established that there are two transitions for the scaling behaviour of the Nusselt number as a function of the Rayleigh number. We found that the rotation cause the first transition to happen at a higher Rayleigh number, as compared with the non-rotating case. Within statistical uncertainties, the obtained results are in agreement with the ones obtained by Grossman and Lohse, and by Ashkenazi and Steinberg.

Acknowledgements

My first thanks go to Professor Andreas Tilgner and all the staff of the Geophysics Institute of Göttingen University for hosting me at their department and for the opportunity of writing my thesis there. In particular I am grateful to PhD student Kevin Luedemann for the time that he spent in explaining me a wide set of topics related with my thesis and more, demonstrating the attitude to be a great professor.

Thanks to Professor Jaan Kalda for his *Fully Developed Turbulent Lectures*, for showing us how intuition based analysis leads to play with equations and proofs more than by treating those as monolithic entities which are not meant to be disassembled.

I am thankful to my parents, for supporting my studies, encouraging me to improve myself and for giving the best example of how learning shall be a daily activity.

Thank you to my sister Nena for always advising and exorting me, for teaching how to be more effective in decision making. Thank you also for sharing all your theoretical wisdom and showing me how to apply it to everyday life as well.

List of acronyms, constants and dimensionless numbers

BC	Boundary Conditions
BL	Boundary Layer
MPI	Message Passing Interface
NS	Navier-Stokes
PyPlot	Python Matplotlib
RB	Rayleigh-Bènard
SEM	Spectral Element Method

α [K^{-1}]	Thermal expansion coefficient
g [m$\cdot$ s^{-2}]	Gravity acceleration
λ [W (m K)$^{-1}$]	Thermal conductivity
L [m]	Length scale
κ [m$^2\cdot$ s^{-1}]	Thermal diffusivity
ρ [Kg $\cdot$ m^{-3}]	Density
ρ_0 [Kg $\cdot$ m^{-3}]	Density at reference temperature T_0
Ω [s^{-1}]	Angular velocity of rotating reference frame
c_p [J (Kg K)$^{-1}$]	Specific heat

Ek	Ekman
Eu	Euler
Fr	Froude
Gr	Grashof
Ma	Mach
Nu	Nusselt
Pr	Prandtl
Ra	Rayleigh
Re	Reynolds

Table of Contents

List of Figures

1. Introduction

Rayleigh-Bènard convective problems have been analysed for decades to explicit their dynamic behaviors, their morphological and topological patterns. RB convection shows behaviors which explanations require the use of mathematical and geometrical tools which one would not expect.

For example, with the right combination of parameters as aspect ratio, viscosity and temperature difference, it has been found that, at the stable equilibrium of the convective cells, their shapes form an exagonal pattern [Varé et al., 2020] (see Figure 1 for an example).

The theoretical explanation of this pattern was found to be coming from a minimization problem: indeed exagons are the geometrical figure that minimize the perimeter of the tessellation of a plane.

The aim of this thesis is to validate the behavior of RB convection with high Prandtl number, varying Ekman and Rayleigh numbers. Prandtl number is the ratio of momentum diffusivity to thermal diffusivity. High Prandtl number fluids are typically analysed in geophysics, due magma and earth mantle high viscosity, but also in some industrial applications of silicone oils. It has been confirmed that for large Prandtl number, Nusselt number and kinetic energy are independent of Prandtl number. Moreover, increasing Ekman number leads to a reduction of the first transition Rayleigh number, indicating that rotation is performing as inhibitor of convection onset.

Scaling laws for Nusselt, Reynolds and Peclet numbers are found. The Nusselt number scaling laws are in line with previous literature, in particular from Ashkenazi and Steinberg[Ashkenazi and Steinberg, 1999]. Related works have been conducted regarding heat transport in RB convection in rotating systems [Schmitz and Tilgner, 2009], analysing transitions from laminar to turbulent flows varying the given parameters (Pr,Ek,Ra) and the heat transport by monitoring the Nusselt number (Nu) [Schmitz and Tilgner, 2010].

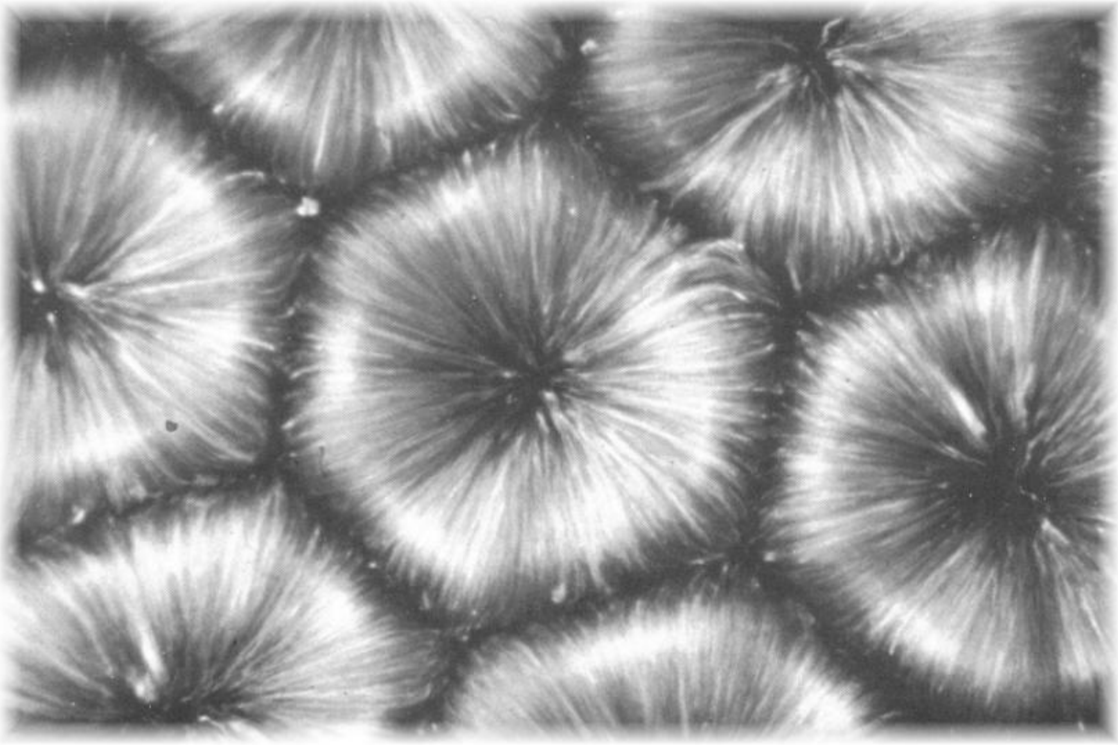

Figure 1. *RB exagonal cells. Picture from NOAA Lab.*

2. Theoretical background

In order to have a better understanding of the phenomena involved in this study, we will go through the theory on which the numerical simulations are based. This summary will start with some general definition of convective motions and their instabilities, going through an overview of Navier-Stokes equations' terms and their numerical implementation, finishing with the meaning of dimensionless numbers and the features of Spectral Methods.

2.1 Convection

In fluid mechanics, convection is defined as the motion of a fluid driven by density difference. Convective phenomena are a pattern of fluid flows that occur due to the combined effects of material property heterogeneity and body forces on a fluid, most commonly density and gravity [Munson et al., 2009]. Another cause of convective phenomena is difference in other properties, surface tension in the Marangoni effect [Tritton, 2012].

Free convection happens because "hot fluid tends to rise" [Tritton, 2012]. Indeed the density variation, that is causing the buoyancy force gradient in the fluid domain, arise due to temperature variation. The model that we are using assumes incompressible flow, where the density is not function of the pressure. In particular, density is function only of temperature. This is known as Bousinnesq approximation (see Section 2.2.1)

Despite the complexity of the hydrodynamics equations, some simple flow patterns are allowed as stationary solutions. Such stationary flows can happen only inside certain ranges of characterizing parameters [Chandrasekhar, 2013]

2.1.1 Rayleigh-Bènard

A layer of fluid is bounded by two horizontal rigid planes at distance d apart and at different constant and uniform temperatures T_1 (up) and T_2 (down), with $T_2 > T_1$. This is called the Rayleigh-Bènard configuration.

There are variations on the theme, e.g. with different boundary conditions, or by replacing the boundary heat source with an internal one. The system evolution does not necessarily undergo a convective motion, since viscosity and thermal diffusivity of the fluid tend to prevent the appearance of convection. Only when the temperature gradients are large enough, then the layer becomes unstable [Tritton, 2012].

Rayleigh-Taylor thermal instability have been analysed by Rayleigh in 1916, who derived a theoretical requirement for convective motion. He showed that thermal instability appears when the ratio of the buoyancy force to the viscous one is exceeding a certain critical value. This ratio is called Rayleigh number:

$$\mathrm{Ra} = \frac{g\alpha L^3 \Delta}{\kappa\nu} \tag{2.1}$$

where $\Delta = T - T_{wall}$ here denotes the temperature difference between the imposed boundary conditions temperatures, which will be set unitary. The instabilisation of the fluid at rest can be seen in the following pictures, obtained from some preliminary 2D simulation with Pr $= 7$ in non-rotating domain with higher aspect ratio. Figure 4 shows how the instability leads to formation of those waves which transforms in plumes dividing each Rayleigh-Bènard convective cells. The video from which those snaps are captured shows how the lateral plumes in Figure 5 are in a velocity limit cycle. It can also be seen how the mode in which the initial stratification instabilise is associated to a very short wavelength, and while the instabilisation evolves, the modes compact themselves in lesser and lesser plumes until the final cells configuration.

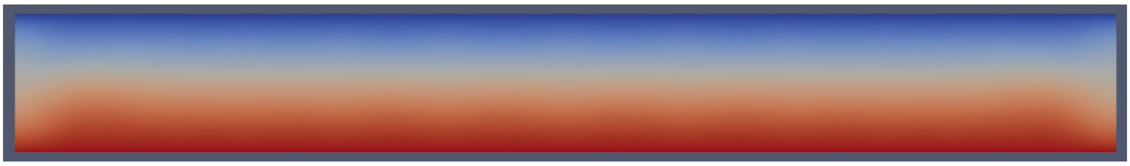

Figure 2. Rayleigh-Taylor instabilisation, $t = 0$

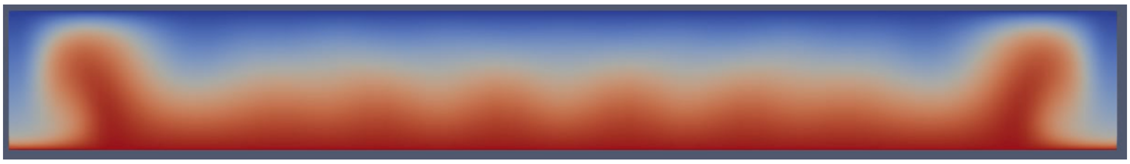

Figure 3. Rayleigh-Taylor instabilisation, t_1

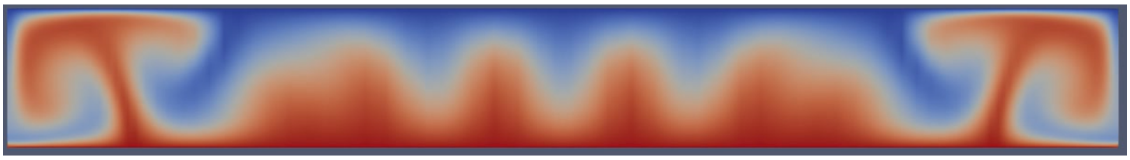

Figure 4. Rayleigh-Taylor instabilisation, t_2

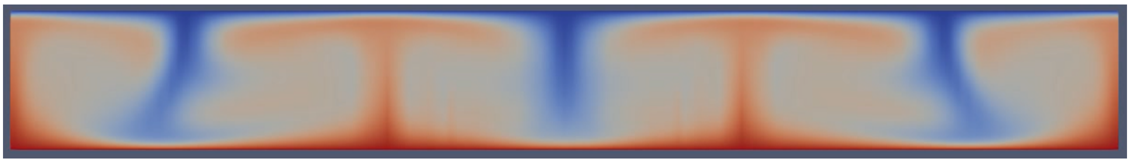

Figure 5. Rayleigh-Taylor instabilisation, t_3

2.1.2 Grossman-Lohse unifying theory

Many studies have been conducted in this field during the 20^{th} century. Davis have studied RB convection for air cells with Pr ≈ 1. He found a scaling law for this particular value of Prandtl number: Nu $\approx$ Ra$^{\frac{1}{4}}$ [Davis, 1922] . However, in these early experiments only relatively small Rayleigh numbers Ra $< 10^8$ were achieved. A detailed description of the history of progresses that have been done during the 20^{th} century in this field can be found in the first of the two papers by Grossman and Lohse [Grossmann and Lohse, 2000].
In the series of those two articles the authors present a consistent unifying theory for RB convection [Grossmann and Lohse, 2000] [Grossmann and Lohse, 2001].

The first article The authors proposed a scaling theory of the Nusselt and Reynolds numbers in strong Rayleigh–Benard convection [Grossmann and Lohse, 2000]. Here the control parameters are the Rayleigh number and the Prandtl number; the system responds with the Nusselt number (the dimensionless heat flux) and the Reynolds number (the dimensionless large scale velocity U). The authors studied the dependence of the scaling laws on the convective regime. The regime's dependence is modelled as function of range of the Prandtl number. For example in the case of the "Kraichnan regime", which corresponds to medium Pr, the parameters follow the scaling laws:

$$\mathrm{Nu} \approx \mathrm{Ra}^{\frac{1}{2}}\mathrm{Pr}^{\frac{1}{2}} \qquad ; \qquad \mathrm{Re} \approx \mathrm{Ra}^{\frac{1}{2}}\mathrm{Pr}^{-\frac{1}{2}}$$

The comparison with our results will be done with the regime corresponding to the highest considered Prandtl number range. This result will be found to be still under the treshold over which the Nusselt number becomes independent of Prandtl number. This scenario will be tackled in the second paper (see Paragraph 2.1.2) The results presented by Grossman and Lohse are the following:

$$\mathrm{Nu} \approx \mathrm{Ra}^{\frac{3}{7}}\mathrm{Pr}^{-\frac{1}{7}} \qquad ; \qquad \mathrm{Re} \approx \mathrm{Ra}^{\frac{4}{7}}\mathrm{Pr}^{-\frac{6}{7}} \tag{2.2}$$

The second article 's aim is to review scaling laws including larger Prandtl number convection. The key question is to understand how the dependences Nu (Ra , Pr) and Re (Ra , Pr) are varying at high Prandtl number [Grossmann and Lohse, 2001]. One important result of the mentioned paper is that over a certain treshold, the Nusselt number is found to be independent of Prandtl number. However, for fixed Rayleigh numbers Ra, a maximum in the Nu (Pr) dependence has been predicted. This allowed a more detailed description of the transitions between the various scaling regimes. Another achievement of this paper has been to decompose energy and thermal dissipation rates into their boundary layer and bulk contributions. This topic will not be discussed here as it falls out of the scope of this thesis.

2.2 Model and equations

The problem have been settled up with some hypotheses: first of all it has been assumed that the fluid is incompressible. Hence the density of the fluid was independent of pressure. Though, the density is dependent of the temperature instead, where the function describing this dependency is assumed to be linear:

$$\rho(T) = \rho_0 + (T - T_0) \cdot \alpha \tag{2.3}$$

where α is the thermal expansion coefficient of the considered fluid. With this hypotheses we can describe temperature as an active scalar, which is a quantity that while being transported is also affecting the flow field; whereas a passive scalar is not leading to any change in the flow.

2.2.1 Boussinesq approximation

Fluids properties are normally functions of temperature. Even when temperature variations are small, those can cause the motion of the fluid, as it happens in free convection (see Section 2.1)

If the density variation is not large, we can introduce the following approximation: density is considered constant in the unsteady and convection term, while it is treated as a variable only in the gravitational term. Also, variation of all fluid properties other than temperature, and consequent density variation, are ignored completely. Density variation is considered when it gives rise to a gravitational buoyancy.

In general, $\rho = f(T)$ hence $\nabla \cdot \mathbf{u} = f(\frac{\mathrm{d}T}{\mathrm{d}t})$ (see Section 2.2.2).

The continuity equation (see Equation 2.4) is then used in its constant density form for incompressible flows: $\nabla \cdot \mathbf{u} = 0$

Apart of the interpretation by analysing the effect on the terms of NS equations, it is possible to see also a physical interpretation. It assumes that variations in density have no effect on the flow field, except that they give rise to buoyancy forces. For example, an increment of temperature does not imply a local expansion of the fluid which cause a divergent velocity field.

We can express the linearization of the density in function of the temperature as in Equation 2.3 to obtain buoyancy force:

$$(\rho - \rho_0)\mathbf{g} = -\rho_0 \mathbf{g} \alpha (T - T_0)$$

where α is the coefficient of volumetric expansion. This approximation leads to errors of the order of 1% if temperature difference is below a certain treshold. The latter is 2° for water ad 15° for air.

2.2.2 Continuity

The continuity equation in its integral form impose the balance between the temporal variation of the considered quantity (in this case mass), the flux q through the domain boundary and the sources of the quantity inside the domain. In 3D case, referring to a fluid with mass, it takes the following form:

$$\frac{\mathrm{d}}{\mathrm{d}t} \int_{\Omega} \rho \, dV = \int_{\Omega} q \, dV - \int_{\partial\Omega} \mathbf{u} \cdot \hat{\mathbf{n}} \, dS$$

We can shrink the domain by limit to a point and obtain the differential form of the continuity equation:

$$\frac{\partial \rho}{\partial t} = q - \nabla \cdot \mathbf{u} \tag{2.4}$$

where $\nabla\cdot$ is the divergence operator. It expresses the net flux of quantity through the boundary of an infinitesimally small domain. Thanks to incompressibility assumption we can state that the divergence of the velocity field will be equal to the mass source function, assumed to be zero, since mass is not self-generating or vanishing in our domain. Moreover, the system has been imposed to be closed in this problem, hence all the lagrangian particles are remaining the same during the time evolution.

2.2.3 Heat transport

Heat diffusion equation relies on the Laplace operator. The heat flux between two particles is modelled as proportional to the temperature difference. The physical meaning of the Laplace operator in a discrete stencil is that the temporal variation of the temperature is proportional to the average of temperature differences between a fluid particle and its infinitesimally close particles (see Equation 2.2.3).
In the context of continuums, the temperature difference between particles is replaced by the spatial derivative, and the time interval by the time derivative. For sake of simplicity we consider the 2D case in Cartesian coordinates, with $T = T(x, y)$.

$$\frac{\partial T}{\partial t} = \lambda\Big(\frac{\partial^2 T}{\partial x^2} + \frac{\partial^2 T}{\partial y^2}\Big) = \lambda \nabla^2 T \tag{2.5}$$

Or, in short notation

$$\dot{T} = \lambda\, \Delta T$$

As we mentioned before, the laplace operator cause the averaging the directional derivatives to appear. This attribute is particularly intuitive when discretizing the problem: the heat equation in a 2D Cartesian discretized domain have the following form.

$$\nabla^2 T = \frac{T(i+1,j) + T(i-1,j) + \ T(i,j+1) + T(i,j-1) \ - 4T(i,j)}{h^2}$$

where (i, j) are the spatial discretization indexes for the domain in (x,y) and h is the spatial discretization step.
For simplicity here we have considered the isotropic case, where $h_x = h_y$

Heat advection equation relates the spatial gradient of temperature, the fluid velocity field and the temperature temporal derivative. Its general form, for compressible flow can be written as:

$$\frac{\partial T}{\partial t} = -\mathbf{u} \cdot \nabla T + \frac{Q}{\rho c_p} \tag{2.6}$$

where Q is a heat source function and c_p is the specific heat.
If we assume the hypotheses of incompressible flow and no heat soure function, the Equation 2.6 becomes:

$$\frac{\partial T}{\partial t} = -\mathbf{u} \cdot \nabla T \tag{2.7}$$

Heat advection-diffusion Thanks to the linearity of the model that relates heat flux and temperature derivative, we can combine the Equations 2.5 and 2.7 to get the heat advection-diffusion equation for incompressible flows :

$$\frac{\partial T}{\partial t} = \lambda \nabla^2 T - \mathbf{u} \cdot \nabla T \tag{2.8}$$

Or, in expanded form, in 3D:

$$\frac{\partial T}{\partial t} = \alpha\Big(\frac{\partial^2 T}{\partial x^2} + \frac{\partial^2 T}{\partial y^2} + \frac{\partial^2 T}{\partial z^2}\Big) - \big(u, v, w\big) \cdot \big(\frac{\partial T}{\partial x}, \frac{\partial T}{\partial y}, \frac{\partial T}{\partial z}\big)$$

Euler and Navier-Stokes equations

Pressure force is generated by difference between the normal stress acting on two sides of the infinitesimal cube. In one dimension it is the pressure spatial derivative, in more than one dimension it is generalized with the gradient of the pressure. Again we can see its meaning by discretizing in a 5 points symmetric stencil in the 2D case:

$$F_p(i,j) = \nabla \cdot \sigma(i,j) = \nabla p \otimes (h_y, h_x) = (\frac{\partial p}{\partial x} \cdot h_y, \frac{\partial p}{\partial y} \cdot h_y) =$$

$$= \frac{p(i+1,j) - p(i-1,j)}{2\,h_x} h_y + \frac{p(i,j+1) - p(i,j-1)}{2\,h_y} h_x$$

where h_x is the discretization step along x axis , and similarly for y axis.

Viscous force can be seen as the diffusion of linear momentum. Recalling the consideration done in the case of heat diffusion in Equation 2.5, we introduce the Laplace operator to express the viscous force:

$$F_v(i,j) = \nabla \cdot \tau(i,j) = \mu \nabla^2 \mathbf{u}$$

where its numerical 5 points stencil scheme is analogue to the heat diffusion case, hence it is not reported individually. The viscous force can be formalized also by mean of the divergence of the deviatoric stress $\nabla \cdot \tau$, where

$$\tau = \mu(\nabla \mathbf{u} + \nabla \mathbf{u}^T)$$

Buoyancy force arises as difference between the body force and the parallel component of the net pressure force. In the simplest case the body force is gravitational (no rotations involved), hence the buoyancy is resulting of $\rho\, g$ and the vertical derivative of pressure $\frac{\partial p}{\partial z}$.

Rotating frame associated forces We can relate the acceleration of a particle with respect to an inertial reference frame to the acceleration of the same particle with respect to a rotating reference frame. [Tritton, 2012]

$$\left(\frac{D\mathbf{u}}{Dt}\right)_I = \left(\frac{D\mathbf{u}}{Dt}\right)_R + \boldsymbol{\Omega} \times (\boldsymbol{\Omega} \times \mathbf{x}) + 2\boldsymbol{\Omega} \times \mathbf{u_R} \tag{2.9}$$

Coriolis force arises when we are using a reference frame that is in rotation with respect to an inertial reference frame. Its expression is

$$-2\rho(\Omega \times \mathbf{u})$$

where Ω is the angular velocity of the non-inertial reference frame with respect to the inertial one; $\mathbf{u}$ is the velocity of the object with respect to the non-inertial reference frame.

Incompressible Euler equation is obtained by substituting the expression of the divergence of the stress tensor in the Cauchy momentum balance equation by its expression:

$$\nabla \cdot \sigma = \begin{pmatrix} \frac{\partial \sigma_{xx}}{\partial x} \\ \frac{\partial \sigma_{yy}}{\partial y} \\ \frac{\partial \sigma_{zz}}{\partial z} \end{pmatrix} \quad ; \quad \frac{\mathrm{d}\mathbf{u}}{\mathrm{d}t} = \frac{1}{\rho} \nabla \cdot \sigma + \mathbf{g}$$

Here we see only the contribute of the diagonal terms, which represent the axial stresss (gradient of pressure). The non-diagonal terms represent the tangential stresses (viscous) that here are neglected since Euler's equation is referred to inviscid flow. Physically it considers the acceleration of a fluid particle due to pressure and volume forces only.

$$\frac{\partial \mathbf{u}}{\partial t} + (\mathbf{u} \cdot \nabla)\mathbf{u} = -\frac{\nabla p}{\rho} + \mathbf{g} \tag{2.10}$$

Incompressible Navier-Stokes equation is the generalization of the Euler equation in the case of viscid flow: indeed we can see that we have added the non-diagonal terms in the stress tensor, which represent the viscosity term in the Euler Equation 2.10. Here the divergence of the stress tensor is equal to the sum of the pressure gradient and the laplacian of the velocity field which express the tangential viscous term.

$$\nabla \cdot \sigma = -\frac{\nabla p}{\rho} + \mu \nabla^2 \mathbf{u}$$

$$\nabla \cdot \sigma = \begin{pmatrix} \frac{\partial \sigma_{xx}}{\partial x} + \frac{\partial \sigma_{yx}}{\partial y} + \frac{\partial \sigma_{zx}}{\partial z} \\ \frac{\partial \sigma_{xy}}{\partial x} + \frac{\partial \sigma_{yy}}{\partial y} + \frac{\partial \sigma_{zy}}{\partial z} \\ \frac{\partial \sigma_{xz}}{\partial x} + \frac{\partial \sigma_{yz}}{\partial y} + \frac{\partial \sigma_{zz}}{\partial z} \end{pmatrix}$$

Then we get the NS equation in vector form, that must be expanded along the three dimensions to be implemented numerically.

$$\frac{\partial \mathbf{u}}{\partial t} + (\mathbf{u} \cdot \nabla)\mathbf{u} = -\frac{\nabla p}{\rho} + \nu \nabla^2 \mathbf{u} + \mathbf{g} \tag{2.11}$$

If we introduce the rotation of the reference frame, we can see the terms associated to Coriolis and centrifugal forces appearing into NS equation: the added terms were seen in Equation 2.9. This leads to:

$$\frac{\partial \mathbf{u}}{\partial t} + \mathbf{u} \cdot \nabla \mathbf{u} = -\frac{1}{\rho}\nabla p - \mathbf{\Omega} \times (\mathbf{\Omega} \times \mathbf{r}) - 2\mathbf{\Omega} \times \mathbf{u} + \nu \nabla^2 \mathbf{u} \tag{2.12}$$

On the RHS of the Equation 2.12 the second term represent the centrifugal force, while the third term is the Coriolis force.

2.2.4 Vorticity and poloidality

Vorticity ω is defined as the curl of the velocity vector field. Hence it is a vector and it is defined in dimension equal to 2 or 3

We can compute for 2d case:

$$\omega_z = \frac{\partial v}{\partial x} - \frac{\partial u}{\partial y}$$

and for the 3D case:

$$\omega = \nabla \times \mathbf{u} = \hat{\imath}\Big(\frac{\partial w}{\partial y} - \frac{\partial v}{\partial z}\Big) + \hat{\jmath}\Big(\frac{\partial u}{\partial z} - \frac{\partial w}{\partial x}\Big) + \hat{k}\Big(\frac{\partial v}{\partial x} - \frac{\partial u}{\partial y}\Big) \tag{2.13}$$

Poloidality of the flow have been computed inside the simulations loops. Poloidal components have been computed in the following way:

$$P = \begin{pmatrix} P_x \\ P_y \\ P_z \end{pmatrix} = \begin{pmatrix} \frac{\int_V \omega_x^2}{\int_V \omega_y^2 + \int_V \omega_z^2} \\ \frac{\int_V \omega_y^2}{\int_V \omega_x^2 + \int_V \omega_z^2} \\ \frac{\int_V \omega_z^2}{\int_V \omega_x^2 + \int_V \omega_y^2} \end{pmatrix} \tag{2.14}$$

The computation have been implemented in the **.usr** file by adding the following lines. The syntax belongs to Fortran 77.

```
c     Compute Poloidal and Toroidal (helmoltz decomposition)
      if(mod(istep,100).eq.0)then
       call gradm1(DvxDx,DvxDy,DvxDz,vx)
       call gradm1(DvyDx,DvyDy,DvyDz,vy)
       call gradm1(DvzDx,DvzDy,DvzDz,vz)
intomegaxsq= glsc3( DvzDy-DvyDz , DvzDy-DvyDz , bm1,nv)
intomegaysq= glsc3( DvxDz-DvzDx , DvxDz-DvzDx , bm1,nv)
intomegazsq= glsc3( DvyDx-DvxDy , DvyDx-DvxDy , bm1,nv)
pol_var_x=intomegaxsq/(intomegazsq+intomegaysq)
pol_var_y=intomegaysq/(intomegaxsq+intomegazsq)
```

```
pol_var_z=intomegazsq/(intomegaxsq+intomegaysq)
      endif
```

The subroutine **gradm1** computes the partial derivatives of the three velocity components, then the volume integral of the vorticity is done in the **glsc3** subroutine, giving as input already the curl structure to express the vorticity from the partial derivatives of the velocity field. Finally, the ratios are imposed in the last three lines beginning with **pol_var**.

2.3 Dimensionless equations

2.3.1 Dimensionless Navier-Stokes

We start from a generic dimensional incompressible NS equation:

$$\rho\Big(\frac{\partial}{\partial t} + (\mathbf{u}\cdot\nabla)\Big)\mathbf{u} = -\nabla p + \mu\nabla^2\mathbf{u} + \rho\mathbf{g}$$

It is possible to make dimensionless the NS equations in different ways. For each problem it will be convenient to proceed in different ways. A quite standard way is the following, where Euler, Froude and Reynolds number are involved since those are associated respectively to pressure, gravity waves and viscous forces. [1]

$$\frac{\partial\mathbf{u}}{\partial t} + \big(\mathbf{u}\cdot\nabla\big)\mathbf{u} = -\mathrm{Eu}\,\nabla p + \frac{1}{\mathrm{Fr}^2}\,\mathbf{g} + \frac{1}{\mathrm{Re}}\,\nabla^2\mathbf{u}$$

For our problem the NS equation is involving also rotation related terms, hence the Equation 2.12 has been made dimensionless in the following way [Schmitz and Tilgner, 2010].

$$\frac{\partial\mathbf{u}}{\partial t} + (\mathbf{u}\cdot\nabla)\mathbf{u} + 2\frac{\mathrm{Pr}}{\mathrm{Ek}}\hat{\mathbf{z}}\times\mathbf{u} = -\nabla p + \mathrm{Pr}\,\nabla^2\mathbf{u} + \mathrm{Ra}\,\mathrm{Pr}\,T\hat{\mathbf{z}} \tag{2.15}$$

In this equation the dimensionless numbers combinations are representing the following phenomena:

- $\frac{\mathrm{Pr}}{\mathrm{Ek}}$ Coriolis force
- $-\nabla p$ Pressure gradient given from gravity and centrifugal force (see description of Equation 3.3)

---

[1] See Appendix 4

- Pr Viscous behavior is proportional to Prantdl number
- Ra Pr is the product involved to take account of buoyancy given from thermal expansion

which are exposed since not all their roles in every term are found to be intuitive.

2.3.2 Dimensionless numbers

Reynolds number is the ratio of inertia force to viscous force:

$$\mathrm{Re} \equiv \frac{\text{inertia}}{\text{viscous}} \propto \frac{\rho u \frac{\partial u}{\partial x}}{\mu \frac{\partial^2 u}{\partial x^2}} \propto \frac{\rho U^2 l}{\mu U l^2} = \frac{U\,l}{\nu} \tag{2.16}$$

The equality of Re is a necessary for dynamic similarities in which viscous forces are relevant.

Prandtl number is the ratio of momentum to heat diffusivity:

$$\mathrm{Pr} \equiv \frac{\text{momentum diffusivity}}{\text{heat diffusivity}} = \frac{\mu\rho}{k\rho C_p} = \frac{\nu}{\alpha} \tag{2.17}$$

It is therefore a fluid property and not a flow variable.

High Prandtl number indicates a fluid with high viscosity and low thermal diffusivity. This corresponds to a diverse set of applications, from silicone oil with Pr≈ 450 for industrial purposes [Busse and Whitehead, 1971], to magma and earth mantle [Kaminski and Jaupart, 2003] in geophysical sciences which are respectively 10^3 and 10^{23} . One of the aims of this study has been identifying the order of magnitude of the treshold of Prandtl number for which the convective patterns stabilize to a flow that is approximately close to Steady Stokes Flow, so that the other parameters of the flows can be obtained with a smaller computational effort. As it will be presented, Pr $= 100$ and Pr $= 300$ give results that satisfy the approximations requirements to allow considering both of them as infinite in the studies of RB convection. Also, the flow will be found to be laminar under a certain treshold of Rayleigh number, which is a function of both Ekman and Prandtl, for low Prandtl number values. For large Pr , the parameters describing the flow become independent from Pr. This result will be presented in the conclusions.

Peclet number in the context of heat transport in fluids is defined as the ratio of the advective transport rate to the diffusive transport rate. Mathematically it can be expressed as the product of Reynolds and Prandtl numbers:

$$\mathrm{Pe} \equiv \frac{\text{heat advection}}{\text{heat diffusion}} = \mathrm{Re} \cdot \mathrm{Pr} = \frac{U\,L}{\nu}\frac{\nu}{\alpha} = \frac{U\,L}{\alpha} \tag{2.18}$$

The direct proportionality of Peclet number to Reynolds number can be intuitively seen using turbulence as the lecture key phenomena: as we know, Reynolds number is an indicator of how the flow is laminar or turbulent. For large Re the velocity field is transporting more heat compared to the same fluid at lower Re since velocity is higher in absolute value and mixing phenomena are leading to a situation where diffusion make solutions smoother in term of high temperature gradients.
Because of the multifractal structure of the mixed solution, which has a layered pattern, the needed heat diffusivity to smooth those temperature gaps decrease since the involved distances tend to zero due to fractality of turbulence. The direct proportionality of Peclet to Prandtl number comes from the presence of the thermal diffusivity at the denominator of both Pr and Pe .

2.3.3 Nusselt number and Boundary Layers

For this thesis has been choosen to use ”Wall” boundary conditions on all the lateral faces of the domain, which in NEK 5000 is the nomenclature for an adiabatic and non-slip BC. Hence in the **.box** file is imposed that the heat exchange at the boundaries is null and the velocity vector of the fluid in the first discrete layer of elements at the boundary is zero too. The velocity BL has been solved by imposing non-slip condition and increasing the mesh density by a hyperbolic tangent function(see Equation 3.1) at the boundaries to allow resolving the flow at the boundaries by mean of the regular NS equations. We have performed an estimation of the value of the parameter which regulates how much the hyperbolic tangent mapping is shrinking the mesh size at the BL. This estimation is done by making an hypothesis on the Nusselt number at the boundary, and deducing the estimated thickness from the estimated Nusselt number.
Nusselt number is estimated as:

$$\mathrm{Nu} = \frac{\alpha L}{\lambda}$$

The Nusselt number is important in this evaluation because it express the ratio of convected heat to conducted one. Note that when Rayleigh number is under a critical treshold, the fluid is thermically stratified due to the stability (buoyancy is dominated by viscosity) hence the heat is only conducted, which corresponds to a Nusselt number $\mathrm{Nu} = 1$

Since in this model has been assumed a non-slip BC , then in the velocity BL the heat is only conducted. Anyway heat is only conducted until the Nusselt number start growing from one, that happens a bit more far from the boundaries than the velocity BL's end. This BL in which heat is only conducted although the velocity is not zero is referred as thermal BL. Note that this relationship between the two boundary layers is not always as here: this is a particular situation because high Prantl number implies high viscosity, that at a relatively low Rayleigh number, keep vorticity dependent only from the macroscopic rotation. Some turbulent behaviour emerged at highest Rayleigh number, and we have seen some eddies rotating along the boundaries. For those simulations at large enough Prandtl number, the velocity BL of Blasius type $\lambda_u \approx \mathrm{Re}^{-1/2}$ has been evaluated as thicker than the thermal BL $\lambda_\theta \approx \frac{1}{2} L \mathrm{Nu}^{-1}$ [Grossmann and Lohse, 2000] .

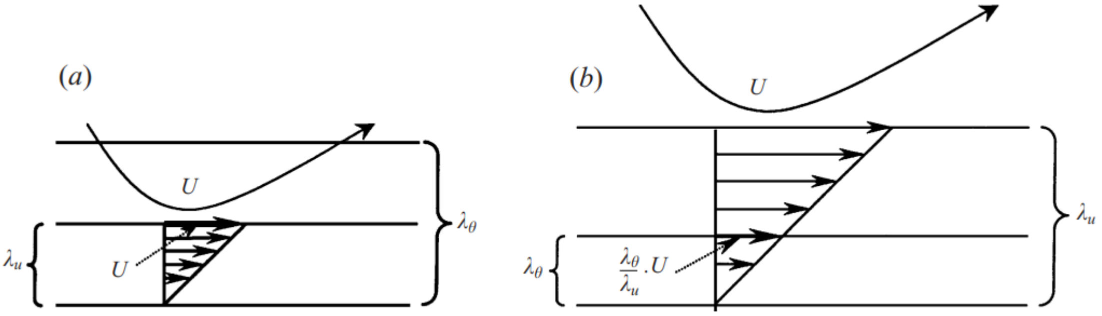

FIGURE 1. Sketch of the boundary layers, (a) for low Pr where $\lambda_u < \lambda_\theta$ and (b) for large Pr where $\lambda_u > \lambda_\theta$.

Hence the heat exchange with the top and bottom walls is a function of the thickness of the boundary layer. For this reason the Nusselt number is used to identify an upper bound to the size of the first mesh layers at the boundaries. This consideration is particularly relevant for top and bottom walls: the lateral walls are adiabatic, hence the mesh size is bounded only by kinematic reasons, but not thermal ones. The thickness of the BL σ is given by the following formula [Grossmann and Lohse, 2000]:

$$\mathrm{Nu} = \frac{L}{2\sigma}$$

Determining the Nusselt number from experiments can be done in two ways: one is relying on the wall heat exchange role of Nu, hence used on the boundaries ; the other is based on the volumetric definition of Nu , hence used in the bulk part of the domain. The first is:

$$\langle \mathrm{Nu} \rangle_W = \langle \frac{\partial T}{\partial z} \rangle_W \tag{2.19}$$

where $\langle \cdot \rangle_W$ denotes the mean value over the wall of the bottom plate. Over the surface of the top plate, that is cold, the Nusselt number value will be the same because of the symmetry of the problem and the linear dependence of buoyancy from temperature.

$$\langle \mathrm{Nu} \rangle_{Vol} = 1 + (\mathrm{Pr}\,\mathrm{Ra})^{0.5} \langle u_z T \rangle_{Vol} \tag{2.20}$$

The mean over the volume of the cell is denoted by $\langle \cdot \rangle_{Vol}$, and the factor $(\mathrm{Pr}\,\mathrm{Ra})^{0.5}$ comes from the adimensionalisation of the velocity field through the free-fall speed. The free-fall speed for this problem can be computed as follow [Verhoeven et al., 2015]:

$$V_f f = \sqrt{\Delta T L \alpha T_r^{-1}} \tag{2.21}$$

2.4 Spectral Element Method (SEM)

SEMs are based on the same idea of the FEM (Finite Elements Method): both methods are using a linear combination of basis functions to approximate the solution. In the FEM the basis functions are defined piece-wise, so each function is non-zero in only one element: this is referred as compact support. Moreover, SEMs are usually easier to implement and on regular geometries require less computational power to obtain higher accuracy than FEM. However, because of their global nature, the matrices associated with step computation are dense and computational efficiency will quickly suffer when there are many degrees of freedom.
Instead, SEM use basis function which are defined non-zero over the whole domain. Indeed, spectral methods connect variables globally while finite elements do so locally.
It relies on writing the trial solution of the differential equation as a sum of certain basis functions and select the expansion coefficients for which the sum approximate the solution well enough. The mentioned expansion is conceptually analogue to the Fourier series, which is a sum of sinusoidal functions. In Spectral Methods, the basis functions are Chebyshev polynomials.
By mean of Spectral Methods it is possible to solve numerically certain differential equations. It is particularly suitable for some particular kinds of differential equations and perform very well in regular geometries. One feature of SEM is the exponential convergence, given at the condition of smoothness of the solution. For this reason, it is not suited to study solutions that have discontinuities (e.g. shock waves) or problems in which there are very high gradients, as in the case of stratified solutions in turbulent patterns that are showing topological properties as Poincaré mappings). Indeed for nonsmooth solutions or larger problems, FEM will generally work better due to sparse matrices and better modelling of discontinuities and sharp bends.

3. Numerical simulations

3.1 The software NEK5000

All the simulations carried out as part of this thesis are performed with the open source software Nek5000. A detailed description can be found in the developer's article [Paul F. Fischer and Kerker
Here we go through a quick overview

Brief history

Nek5000 is a CFD solver based on Nekton 2.0 spectral element code written by Paul Fischer et al. in 1986-1991. [Fischer et al., 2007]
The SEM was introduced in a 1984 article by Patera et al.[Patera, 1984], where it have been used at first to simulate the laminar flow in a channel expansion.
Nekton 2.0 was the first three-dimensional spectral element code and one of the first commercially available codes for distributed-memory parallel processors.

Nek5000 code features

The core of Nek5000 [Paul F. Fischer and Kerkemeier, 2008] is written in F77 and C. It also uses also MPI [MPI, 1994] and some of the subroutines included in LAPACK [Anderson et al., 1999] for eigenvalues computations.
Nek5000 can simulate unsteady incompressible fluid flow with thermal and passive scalar transport. It can handle 2D and 3D domains decribed by isoparametric quad or hex elements. Is also provided with the functionality to compute axial-symmetric flows. It solves the transient incompressible Navier-Stokes equations. Nek5000 also solves the compressible Navier-Stokes equations, but only in a low-Mach approximation, which does not correspond to the anelastic approximation. These can be solved with forced or natural convective heat transfer in both steady-state and time-dependent geometry. It is a time-stepping based code and does not currently support steady-state solvers, other than steady Stokes and steady heat conduction. In the context of this thesis, among the steady-state solvers has been used only the steady Stokes one. Nek5000 is designed for parallel computing using the Message Passing Interface Standard (MPI). In this regard, everything is already built in. Nek5000 uses a semi-implicit Euler-Cromer method (see

Appendix 4.3) for time integration. The semi-implicitness consist in computing the next time step value of the velocity by mean of an explicit method, while the temperature is computed implicitly. This method ensure stability concerning the temperature fluctuations by its implicitness, while allowing a faster computation thanks to the explicitness of the velocity field. This because the velocity field is computed by direct integration instead of solving a linear system.

GLL points (Gauss-Legendre-Lobatto) , or Chebyshev roots, are the locations where the polynomial interpolation based on Chebyshev polynomials is performed. The solution depends sensitively on their number and relative distances. In NEK5000 it is not possible to impose a mapping on their positions to modify the uniformity of their distributions, but is possible to change their density by editing the **.SIZE** file. The number has been set to 5 or 9 as standard, depending on Rayleigh and Ekman number, where the evaluation has been done based on the experience of my supervisor. [1]

The effect of Runge phenomenon, which appeared for some values of polynomial order, is a high amplitude oscillation of the approximating function close to the main nodes, which leads to the crash of the solution process: indeed when the value of the approximating Chebyshev polynomials oscillates over a certain treshold, the program automatically kills the execution. Fortunately, this phenomenon involve the majority of cases where an arbitrary approximated function is given, hence the crash of the simulation was happening in the first few steps, allowing an immediate diagnosis. [2] The peculiarity of the Runge phenomenon is that a coarse spectral mesh can generate less problems than finer ones, counter-intuitively. Indeed the number of spectral nodes has been reduced to two where the problem has sussisted. In the Figures 7 and 6 the spectral nodes have been plotted as red dots along the main mesh. The oscillation can be minimized by using nodes that are distributed more densely towards the edges of the interval, specifically, with asymptotic density. [Berrut and Trefethen, 2004]

3.2 The problem setup

The setup of a simulation on NEK5000 relies on different case files, containing the parameters and execution choices of the simulation.

In NEK5000 is possible to use different sets of equations. For our purpose, we have

---

[1] The evaluation is conducted by heart and not analitically because of the complexity of the Runge phenomenon in this context, since the spectral meshing algorithm is considered as a black-box.

[2] Other oscillatory phenomena did not allow this, and we had to restart some simulations after dozens of computation hours

executed the same simulations with steady Stokes flow hypothesis and with the set of incompressible NS equations.

The aim is to find a treshold of Prandtl number over which incompressible NS and steady Stokes equations give the same results. Prandtl number $\mathrm{Pr} = 100$ already have shown a behavior already very similar to the steady Stokes flow. The treshold have been identified being between $\mathrm{Pr} = 100$ and $\mathrm{Pr} = 300$, depending on the desired accuracy. Indeed at $\mathrm{Pr} = 300$ the temporal evolution and the asymptotic values of the parameters choosen to express the flow characteristics discard from the steady Stokes value by less than 1%

Mesh and Boundary Conditions in the .box file

Mesh In the **.box** file we have specified some of the necessary data: the number of dimensions of the problem have been set to 3 ; the number of the fields involved is 2 (are the velocity vector field and the temperature scalar field) ; the numbers of elements per each of the three sides of the cubic mesh ($= 30 \times 30 \times 30$) and the parameters for their spatial distribution or alternatively, all the nodes of the mesh. The mesh thinness has been changed in base of a trade-off between accuracy and computation costs and stable behavior on the boundaries. This can be done inside NEK5000 that is given with an internal subroutine that can perform arbitrary mappings.

For this thesis have been implemented a Python script generating directly a mesh mapped by a hyperbolic tangent (see Equation 3.1). Here it is presented the printed case file.

```
-3       spatial dimension
2        number of fields
Box
30  30  30    nelx,nely,nelz for Box
0.00e-00 5.57e-03 1.27e-02 2.20e-02 3.38e-02 4.87e-02 6.76e-02
9.12e-02 1.20e-01 1.56e-01 1.98e-01 2.47e-01 3.03e-01 3.65e-01
4.31e-01 5.00e-01 5.69e-01 6.35e-01 6.97e-01 7.53e-01 8.02e-01
8.44e-01 8.80e-01 9.09e-01 9.32e-01 9.51e-01 9.66e-01 9.78e-01
9.87e-01 9.94e-01 1.00e-00 0.00e-00 5.57e-03 1.27e-02 2.20e-02
3.38e-02 4.87e-02 6.76e-02 9.12e-02 1.20e-01 1.56e-01 1.98e-01
2.47e-01 3.03e-01 3.65e-01 4.31e-01 5.00e-01 5.69e-01 6.35e-01
6.97e-01 7.53e-01 8.02e-01 8.44e-01 8.80e-01 9.09e-01 9.32e-01
9.51e-01 9.66e-01 9.78e-01 9.87e-01 9.94e-01 1.00e-00 0.00e-00
5.57e-03 1.27e-02 2.20e-02 3.38e-02 4.87e-02 6.76e-02 9.12e-02
1.20e-01 1.56e-01 1.98e-01 2.47e-01 3.03e-01 3.65e-01 4.31e-01
5.00e-01 5.69e-01 6.35e-01 6.97e-01 7.53e-01 8.02e-01 8.44e-01
8.80e-01 9.09e-01 9.32e-01 9.51e-01 9.66e-01 9.78e-01 9.87e-01
9.94e-01 1.00e-00
W  ,W  ,W  ,W  ,W  ,W          V bc's
I  ,I  ,t  ,t  ,I  ,I          T bc's
```

This solution allows to modify the density distribution of nodes from the bulk of the domain to the boundaries. This is necessary because the boundary layer is where vorticity is being formed. Note that others than the hyperbolic tangent mapping could be used to obtain similar results. The parameter δ in the Equation 3.1 determines whether the mesh is not deformed ($\delta = 1$) or it is deformed such that the density of nodes approaches to infinite at the boundaries and approaches zero in the bulk ($\delta \to 0$).

$$\chi(x) = \frac{\tanh\left(\frac{x-0.5}{\delta}\right)}{\tanh\left(\frac{1}{2\delta}\right)} + 1 \tag{3.1}$$

Here will be used $\delta = 0.3$ as standard value (see Figure 6) , although for high Ra number, the successful run of the program requires to set a finer mesh at the boundary, hence in such cases have been used a smaller value down to $\delta = 0.16$ or in between.

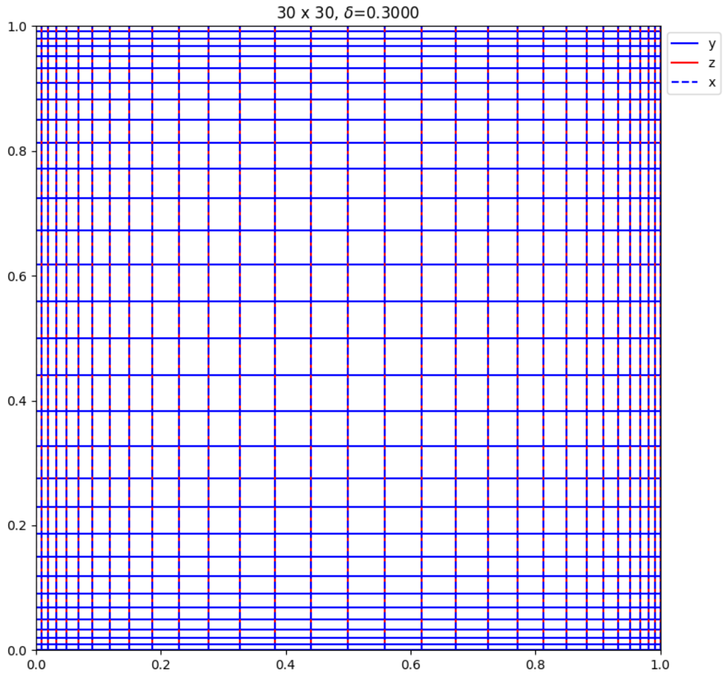

Figure 6. *Mesh with* $\delta = 0.30$ *rendered in 2D with PyPlot*

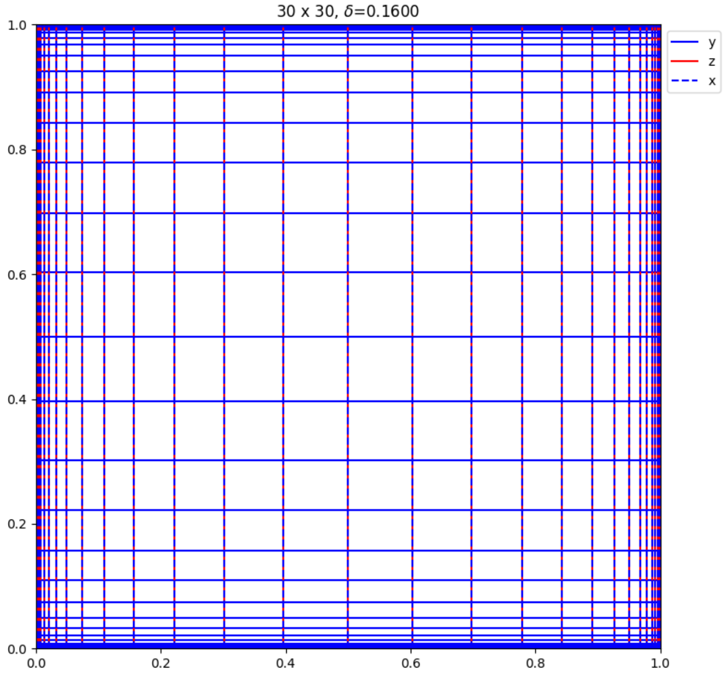

Figure 7. *Mesh with* $\delta = 0.16$ *rendered in 2D with PyPlot*

The last two lines of the **.box** file specify the BCs of the velocity vector field and the transported scalar field, that is temperature. The syntax is structured with six letters, one for each face of the cube in the following order: x^- , x^+, y^- , y^+, z^- , z^+ . For the velocity BCs have been set ”W” as Wall, as specified before, that stands for non-slip BC, then imposing zero flux and zero tangential velocity. This condition impose also that the system is closed to the mass, hence the Lagrangian particles remain the same during the time evolution of the simulation. For the temperature BCs, the lateral walls (along x and z) have been set to ”I” as Insulated, imposing a Neumann BC to zero. The vertical direction has been imposed along y. [3]

Hence the temperature Dirichlet BCs have been imposed on the faces which normal is parallel to the gravity force vector. It simply consist in a unitary temperature difference between the two faces, since the problem has been adimensionalized. In NEK5000 is also possible to impose a Neumann thermal BC, consisting in a heat flux through the surface, but for the scope of this thesis we followed the procedure executed in [Schmitz and Tilgner, 2010, Schmitz and Tilgner, 2009] that was found to be optimal for stability reasons. Indeed the equilibrium is reached faster when Dirichlet BCs are used, since the thermal gradient at the boundary is reaching a steady state when the BL reaches the Dirichlet temperature, which is not happening that rapidly when a thermal flux is imposed. Asymptotic stability is reached anyway, but take around the double of the running time to be fulfilled. [4] This can be interpreted by looking at the stabilization of the Nusselt number along time: after the asympthote is reached, the Dirichlet BC behaves as Neumann BC because the spatial average of the heat flux through the bottom and top faces of the cube remain constant along time. The numerical values have been imposed in the subroutine **userbc** in the **.usr** file.

```
c----------------------------------------------
      subroutine userbc (ix,iy,iz,iside,ieg)
c     Set boundary conditions
      include 'SIZE' ;      include 'TOTAL';      include 'NEKUSE'
      if(y==0) then
          temp=1.0
      end if
      if(y==1) then
```

---

[3] This choice was made because the training have been done with a 2D case, hence the y was already the vertical direction in all case files, hence to keep continuity between the simulations and formulae, we introduced the z-axis as horizontal depth, keeping y-axis vertical

[4] This has been interpreted as a way to keep bounded the energy provided to the system. Indeed we tried some simulations using the same case files but imposing a thermal flux, and we observed a less stable behavior, in particular regarding the kinetic energy.

```
        temp=0.0
    end if
    return
    end
```

.par file

The program allows to set the physical and computational parameters for the simulation inside the **.par** file. For our purpose have been used a Python script that write out the **.par** file with computed viscosity and conductivity parameters ν and α given dimensionless Prandtl and Rayleigh numbers by the equations:

$$\text{Pr} = \frac{\nu}{\alpha}\ ;\ \text{Ra} = \frac{1}{\nu\alpha} \tag{3.2}$$

Among the other parameters we can find

- density: here unitary after the problem has been made dimensionless
- duration of the simulation in both seconds and number of steps
- start time: feature that allows to continue simulations using an arbitrary condition as initial condition
- write interval, that indicates the ratio between the number of steps and the number of data writing
- time stepper: the algorithm that compute the parameter time step for the next data writing interval
- fixed time step, in case we set the time stepper as deactivated
- which set of equation to be used (compressible or incompressible NS , steady Stokes ...)
- CFL target (Courant Friedrichs Lewy): the value of Courant number that the time stepper algorithm seek to fulfill

The Courant condition is particularly relevant for high speed flows with respect to the mesh size. Indeed the flow is imposed to not run across more than one discrete space interval, else the numerical result will consistently diverge from the real value. The Courant number express the ratio between the distance traveled from the flow in a time step to the mesh size, hence it is imposed to be smaller than a critical value which is imposed in the **.par** file.

.usr file

In the **.usr** file it is possible to specify the input values to pre-defined subroutines and to write new ones. As reported for BCs (see Section 3.2) and for poloidal decomposition (see Section 2.2.4), the same have been done for other computations, which are not reported for compactness reason. Those can be found in the appendix (see Chapter 4.3). The other subroutines compute the Peclet number ; the Nusselt number by its two definitions, so the gradient at the boundaries in Equation 2.19 and the volume expression 2.20 ; the kinetic energy and the vorticity. In the same file, also the subroutine to export bulk data of the simulations has been written.

3.3 Simulations

Navier Stokes and steady Stokes in NEK5000

In NEK 5000, NS equations are implemented as following:

- momentum equation

  $$\rho\Big(\frac{\partial \mathbf{u}}{\partial t} + \mathbf{u}\cdot\nabla\mathbf{u}\Big) = -\nabla p + \nabla\cdot\tau + \rho\mathbf{f} \tag{3.3}$$

  where $\tau = \mu[\nabla\mathbf{u} + \nabla\mathbf{u}^T]$ and f is a user defined acceleration. The latter will be used for Coriolis force to implement rotation. Note that the centrifugal term and the gravitational term can be merged into the pressure gradient term thanks to Helmoltz-Hodge decomposition, since those terms are all meant to be expressed as a gradient of a scalar field. This operation is possible thanks to the linearity of the gradient operator, hence the gradient of the sum is equal to the sum of the gradients.
- the continuity equation $\nabla\cdot\mathbf{u} = 0$ can be used thanks to the Bousinnesq approximation (see Section 2.2.1)

In the case of flows dominated by viscous effects, NEK5000 can solve the Stokes equations: the unsteady Stokes equation is

$$\rho\frac{\partial \mathbf{u}}{\partial t} = -\nabla p + \nabla\cdot\tau + \rho\mathbf{f} \tag{3.4}$$

that without time-dependence can be further reduced to

$$-\nabla p + \nabla\cdot\tau + \rho\mathbf{f} = 0 \tag{3.5}$$

In this case, the stationarity hypotheses of the problem simplify consistently the equation by removing the time derivative. This leads to a very low computational cost for its solution. The steady Stokes flow is a very good approximation in case of highly viscous fluid: indeed for the latter is possible to neglect the inertia forces with respect to the viscous forces.

Sets of parameters

The problem have been simulated for every parameters combination from a Cartesian product of the following parameters: Ekman number: $2 \cdot 10^{-4}$, $1 \cdot 10^{-3}$, Infinity $(\omega = 0)$; Prandtl number: $1 \cdot 10^{2}$; $3 \cdot 10^{2}$; steady Stokes $(\rho_I = 0)$; Rayleigh number: 10^3 to 10^9 by steps of one order of magnitude.

Prandtl	Ekman	Rayleigh
100	$1 \cdot 10^{-3}$	10^3
		10^4
		10^5
		10^6
		10^7
		10^8
		10^9
100	$2 \cdot 10^{-4}$	10^3
		10^4
		10^5
		10^6
		10^7
		10^8
		10^9
100	∞	10^3
		10^4
		10^5
		10^6
		10^7
		10^8
		10^9

Prandtl	Ekman	Rayleigh
300	$1 \cdot 10^{-3}$	10^3
		10^4
		10^5
		10^6
		10^7
		10^8
		10^9
300	$2 \cdot 10^{-4}$	10^3
		10^4
		10^5
		10^6
		10^7
		10^8
		10^9
300	∞	10^3
		10^4
		10^5
		10^6
		10^7
		10^8
		10^9

Prandtl	Ekman	Rayleigh
SS	$1 \cdot 10^{-3}$	10^3
		10^4
		10^5
		10^6
		10^7
		10^8
		10^9
SS	$2 \cdot 10^{-4}$	10^3
		10^4
		10^5
		10^6
		10^7
		10^8
		10^9
SS	∞	10^3
		10^4
		10^5
		10^6
		10^7
		10^8
		10^9

Influence and meaning of each parameter

Prandtl number have been settled up to different numerical values, both expected to be high enough so that their behavior could be considered already as Prandtl number was infinity.

An assumption is done in this direction: by imposing high Prandtl number we are implicitly imposing high viscosity, but this is not automatically true, since a high Prandtl number can derive also from a very low thermal conductivity.

The discriminant resides in imposing the Rayleigh number: if the latter is upper bounded from a reasonable high value, then this approximation is fair, and the steady Stokes flow will correspond to high Prandtl number simulated with inertial property. The maximum Rayleigh number that has been simulated was $\mathrm{Ra} = 10^9$ and it still didn't present a significative difference between the steady Stokes and high Prandtl number. To keep a margin, we limited the considered results up to $\mathrm{Ra} = 10^8$ thanks to the fact that the second logarithmic transition happened before that treshold, allowing the interpretation of the results without the need to increase Rayleigh number further.

The comparison have been done with the Steady Stokes simulations, where the inertial term present in the NS equations is neglected, hence the simulation result to be less computationally expensive of about one order of magnitude.

The results show that already $\mathrm{Pr} = 3 \cdot 10^2$ can be considered as infinite Pr, hence we evaluated not necessary to run the simulations for Pr over that value, since the mesh requirements from NEK5000 were difficult to satisfy. It have been conducted the problem for $\mathrm{Pr} = 7 \cdot 10^2$ successfully, but only in 2 dimensions, hence the results are not reported here.

Ekman number 's influence on the problem is given from the effect of Coriolis force on the fluid. The set of values of Ek number have been settled up to: $\mathrm{Ek} = 1 \cdot 10^{-3}$, $\mathrm{Ek} = 2 \cdot 10^{-4}$, and infinite. The associated angular speeds can be obtained for each simulation by using the following equations [Tritton, 2012] :

$$\begin{cases} \mathrm{Ek} = \frac{\nu}{\omega\, L^2} \\ \nu = \sqrt{\frac{\mathrm{Pr}}{\mathrm{Ra}}} \end{cases} \Rightarrow \mathrm{Ek} = \frac{\sqrt{\mathrm{Pr}}}{\sqrt{\mathrm{Ra}}\,\omega L^2} \tag{3.6}$$

The set up of very low Ek numbers, which corresponds to high angular velocities, have been causing instabilities in the results, especially at low Rayleigh numbers. This because the time-stepper adaptive algorithm consider the temperature gradients involved in the

simulations but not the angular velocity of the reference frame. Hence the rotational Mach number is imposing to the time step an upper bound which is not considered in the adaptive time stepper. This condition is analogue to Courant-Friedrichs-Lewy but referred to an angular velocity.
The solution would have been to set manually the time step to very low values until instabilities with their oscillations disappeared. This operation would have required a long time for settling up each simulation due to the long waiting time. For this reason we imposed a lower bound of Ek $= 2 \cdot 10^{-4}$.

One interesting spectrum of phenomena that can appear at higher angular velocities (which we didn't analyse for the given reasons) are the rotational instabilities, that lead to the formation of centrifugal layers given from the break of convective columns which are appearing at very high Rayleigh number, out of the boundaries of this thesis. This phenomena are of particular interest in the field of convective motions in the cores of planets and stars, which also involve Magneto-Hydro-Dynamics(MHD), that is out of our scope.

Rayleigh number The Rayleigh number express the dimensionless buoyancy force.
It is intuitive, and confirmed from theoretical background and simulations, that high thermal gradients are causing larger Rayleigh number to appear, which make the convective motions accelerate faster, then increasing the kinetic energy of the flow (see Plots 16, 17, 18). This velocity increase cause also a Reynolds number increase, which is leading to turbulent patterns.

Tubulence analysis has not been performed since it requires finer meshes in function of the Kolmogorov micro-scales magnitude: indeed to resolve turbulent patterns is necessary to describe the velocity profiles with a very dense mesh grid in order to capture all the smallest velocity gradients down to the viscosity micro-scale. Such an analysis make DNS (Direct Numerical Simulations) to be computationally very expensive, since the run time goes approximately with the cube of the number of discrete elements. Moreover, as suggested from Grossman and Lohse [Grossmann and Lohse, 2000], turbulence is unlikely to appear at Pr $\gg 7$.

Nusselt numbers As pointed out from Grossman and Lohse [Grossmann and Lohse, 2000], at high enough Prandtl numbers, Nusselt number is independent of Prandtl number. This has been one of the two criteria [5] to determine whether the two choosen values of Prandtl

---

[5] the other criterion is the comparison with steady Stokes model

number were to be considered already infinite or not. Indeed, the pairs of simulations that had same Ekman and Rayleigh numbers, differing just for Prandtl, gave the same results in terms of the asymptotical function of Nusselt number logarithm (see Figures from 10 to 15). The equations used to compute the Nusselt number in both its volumetrical and surface definition are reported in Equations 2.20 and 2.19.

Time plots of representative parameters To check the time evolution of the simulation we used some scripts in Python to read from the **.logfile** and plot the presented parameters. When a simulation was proceeding well, it had this nice asympthotical behavior with a little overshooting at the beginning. For example, comparing the Nusselt number in its two ways of being computed, the ”Nu(Gradient)”, which has been indicated as Nu $|w$, does not present the overshooting that appears for the ”Nu(Volume)” (Nu $|v$) because of the velocity boundary layer effect on velocity: indeed it is the advective component which has a peak for the maximal velocity, which happens after an amount of time from the beginning of the simulation in the order of the scale divided by the free fall velocity. Intuitively can be seen as the effect of the ”cumulated buoyancy” at rest which at the beginning has to instabilize the thermal gradient and somehow ”break” the unitary Nusselt number: after the onset of motion, there is a release of the mentioned buoyancy. Here appears the mentioned overshooting, which is then damped from viscous effects. A consistent part of the work has been to set simulation parameters to obtain stable and realistic results. Reducing mesh size and time step does not necessarily solve the problems related with numerical instabilities.

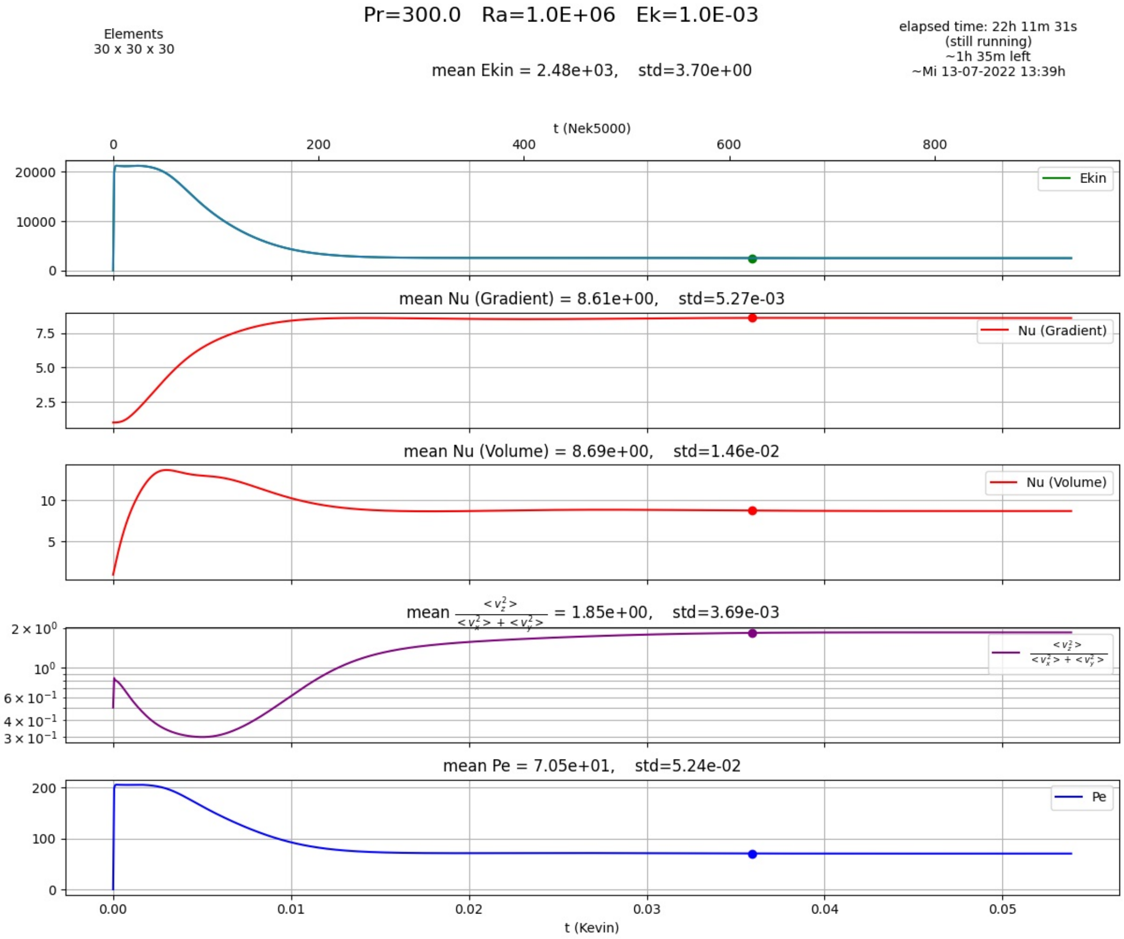

Figure 8. Time plot of: Kinetic energy ; Nusseltlwall ; Nusseltlvol ; $\frac{Ekin\_z}{Ekin\_xy}$; Peclet

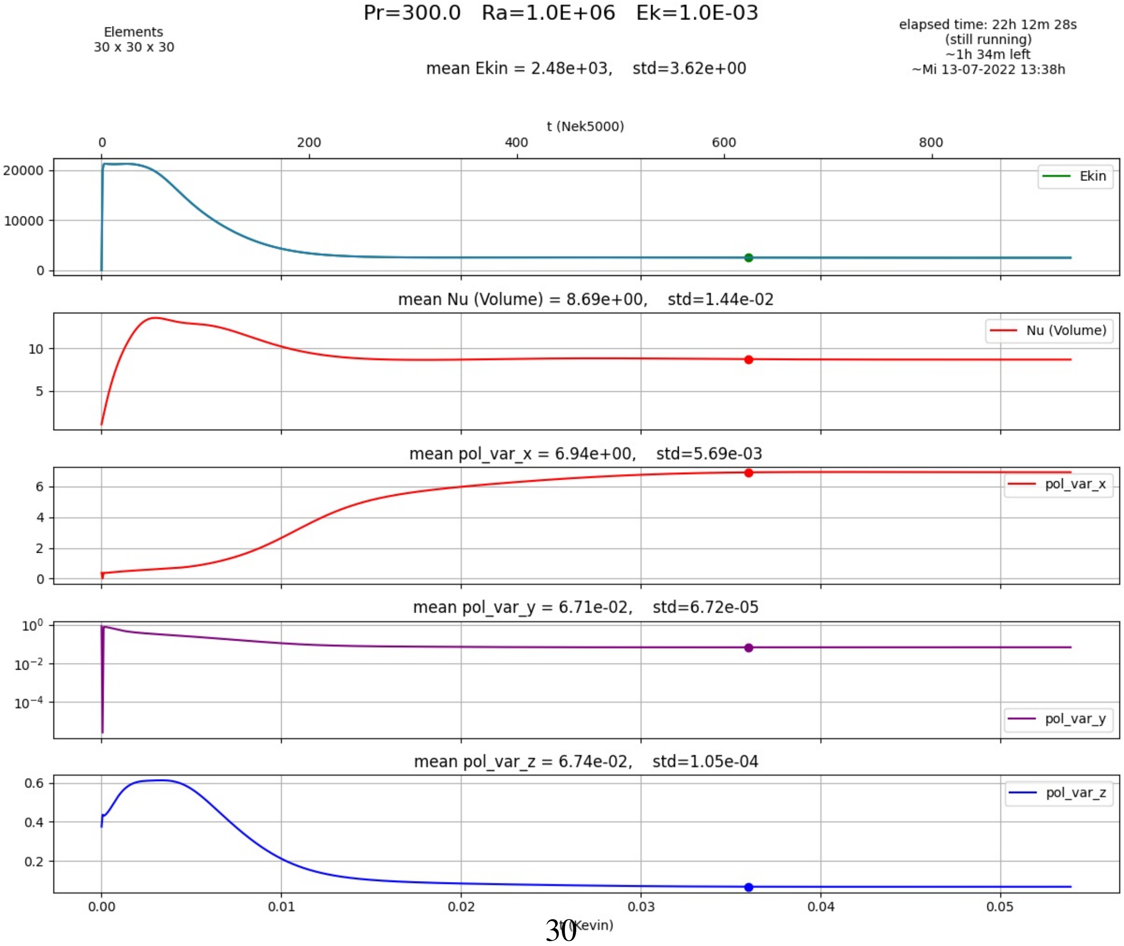

Figure 9. Time plot of: Kinetic energy; Nusseltlvol ; Poloidality along $\hat{x}$,$\hat{y}$ and $\hat{z}$

4. Results analysis and conclusions

4.1 The power laws

In thermal convection the Nusselt number and the kinetic energy are the system response to the choosen input, which are Rayleigh and Prantdl number. Those dependencies $\mathrm{Nu}\,(\mathrm{Ra}\,,\mathrm{Pr}\,)$ and $\mathrm{E_{kin}}(\mathrm{Ra}\,,\mathrm{Pr}\,)$ are found to be very well approximated from exponential laws. The aim of this thesis was to find the scaling exponent and their domains in Rayleigh and Prandtl axis. The results are presented here, and compared with representative values from [Grossmann and Lohse, 2000].

Transitions' Rayleigh number. Transitions between two flow regimes happens at critical values, which are related with the dimensionless numbers that describe the fluid and the flow. In this case, Rayleigh number of transitions depends on Ekman number but not on Prandtl number, as shown in Figures from 10 to 18. The first transition corresponds to the convection onset. Rayleigh number, which represent the ratio of buoyancy force to the viscous force, has to be great enough to cause the instabilisation of the steady state with $\mathbf{u} = 0$ over all the domain. Under this treshold, viscous effects keep the fluid at rest. Two tables are presented: In the first table, the second column contains the value of the first transition Rayleigh number in function of Ekman number. Similarly, the second table present also the Nusselt number at which the second transition happens, which is strictly bigger than one, whereas the first transition happens at $\mathrm{Nu}\ = 1$ by definition.

First transition

Ekman	Rayleigh
∞	$1.3 \cdot 10^3$
$1 \cdot 10^{-3}$	$2.3 \cdot 10^4$
$2 \cdot 10^{-4}$	$1.0 \cdot 10^5$

Second transition

Ekman	Rayleigh	Nusselt
∞	$3 \cdot 10^5$	6.5
$1 \cdot 10^{-3}$	$1.6 \cdot 10^6$	10.2
$2 \cdot 10^{-4}$	$3 \cdot 10^6$	10.3

The uncertainty on the precise value of some numbers has been indicated in blue. This is because pinpointing the transition exactly would have required many more simulations, which was not the main purpose of this thesis.

In the pictures have been plotted the asympthotical behaviour of the scaling laws. In correspondence of the regime's transition it can be observed a sharp variation of slope. Intuitively, the real scaling law do not present those corners, but have a smooth transition between the two regimes. This have been manually plotted in Figure 17 to give an example. All the other plots have to be interpreted consequently.It can be seen how the spread along Rayleigh axis is higher in the case of infinite Ekman number (zero rotation, see Figure 10).In this case it is vaguely identified the second transition, because the scaling coefficient of the first and second regimes are quite similar. Instead, for higher angular velocities, the two regimes are more sharpely identified.

Rotational effects: the first transition which corresponds to the onset of convective motion, for infinite Ek happens in the order of Ra $= 1 \cdot 10^3$. Instead, for the other two values of Ek , it can be seen already from the plots (see Figures 10, 11, 12) that the transition's Ra increases. Hence the values of Ek and Ra at the transition point are found to follow an inverse non-linear proportionality. Their precise relation has not been examined because three cases, each for one Ek value, are not enough to get a relation from a regression. In the same plots it can be seen that the slope of the first ramp is increasing too, whereas the second ramp slope (after the second transition) seem to be less affected from Ek variations than the first ramp slope. The increase of the first ramp imply also that the second transition's Ra is less influenced from Ek variation, since its shift to the right is smoothed from the first ramp slope increase.
The rotation is found to be a factor of inhibition of convection onset.

4.2 Plots

Ra-Nulv

```
Ek            Pr       Regime       Slope
Infinity      100      Ramp1      0.3409
Infinity      100      Ramp2      0.2673
Infinity      300      Ramp1      0.3399
Infinity      300      Ramp2      0.2723
Infinity      SS     Ramp1      0.3498
Infinity      SS     Ramp2      0.2735
1E-03           100      Ramp1       0.5721
1E-03           100      Ramp2       0.2527
1E-03           300      Ramp1       0.5753
1E-03           300      Ramp2       0.2679
```

```
1E-03          SS      Ramp1      0.5723
1E-03          SS      Ramp2      0.2503
2E-04          100      Ramp1      0.6784
2E-04          100      Ramp2      0.2731
2E-04          300      Ramp1      0.6790
2E-04          300      Ramp2      0.2841
2E-04          SS      Ramp1      0.6706
2E-04          SS      Ramp2      0.2696
```

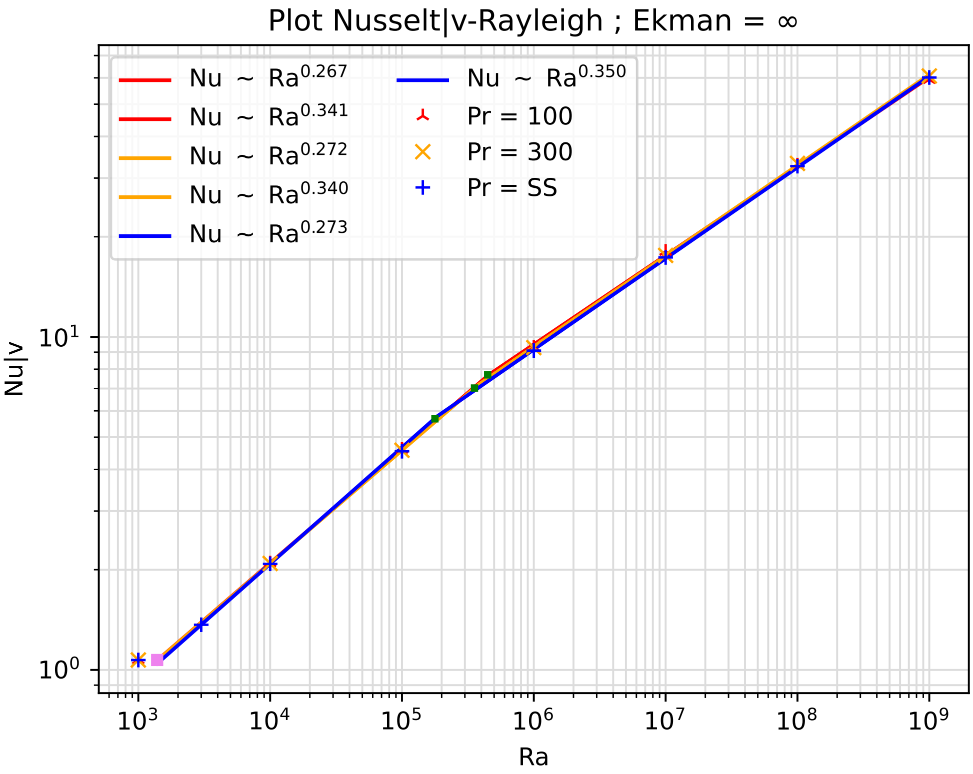

Figure 10. *Plot of the relation between parameters Rayleigh-Nusselt|Vol; Ek* $= \infty$

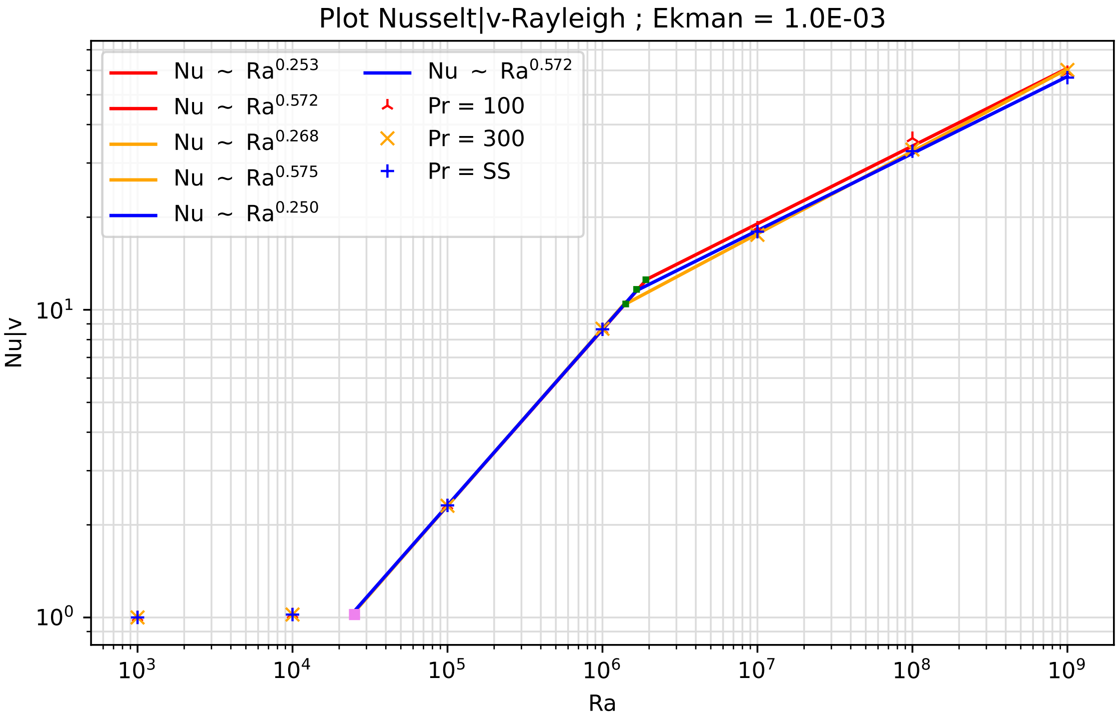

Figure 11. *Plot of the relation between parameters Rayleigh-Nusselt|Vol ; Ek* $= 1 \cdot 10^{-3}$

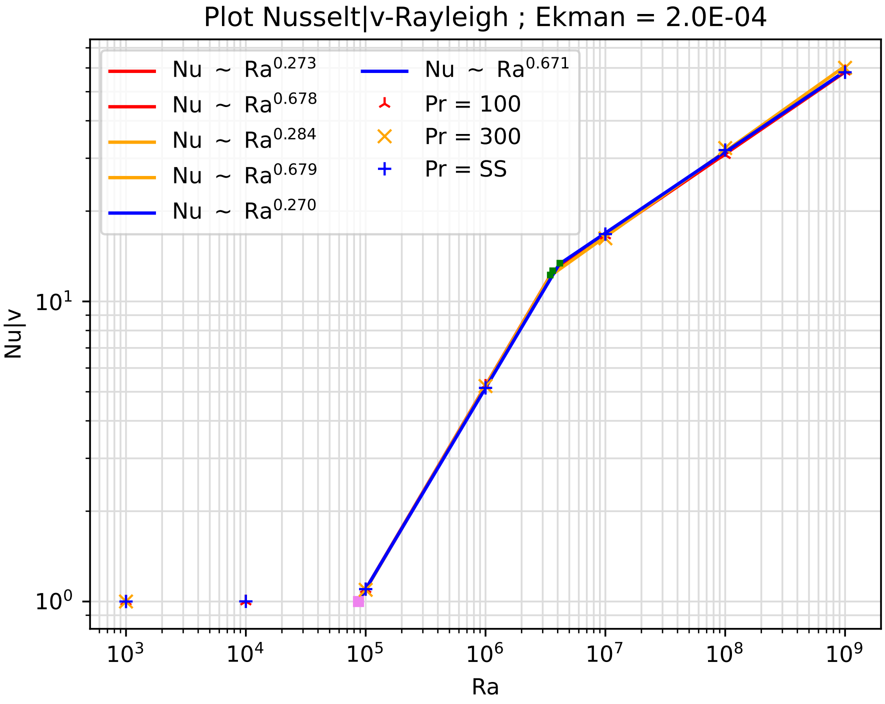

Figure 12. *Plot of the relation between parameters Rayleigh-Nusselt|Vol ; Ek* $= 2 \cdot 10{-}4$

Ra-Nulw

```
Ek           Pr      Regime      Slope
Infinity     100     Ramp1     0.3383
Infinity     100     Ramp2     0.2656
Infinity     300     Ramp1     0.3407
Infinity     300     Ramp2     0.2677
Infinity     SS     Ramp1     0.3484
Infinity     SS     Ramp2     0.2726
1E-03          100     Ramp1     0.5715
1E-03          100     Ramp2     0.2619
1E-03          300     Ramp1     0.5727
1E-03          300     Ramp2     0.2614
1E-03          SS     Ramp1     0.5704
1E-03          SS     Ramp2     0.2587
2E-04          100     Ramp1     0.6726
2E-04          100     Ramp2     0.2688
2E-04          300     Ramp1     0.6765
2E-04          300     Ramp2     0.2777
2E-04          SS     Ramp1     0.6767
2E-04          SS     Ramp2     0.2643
```

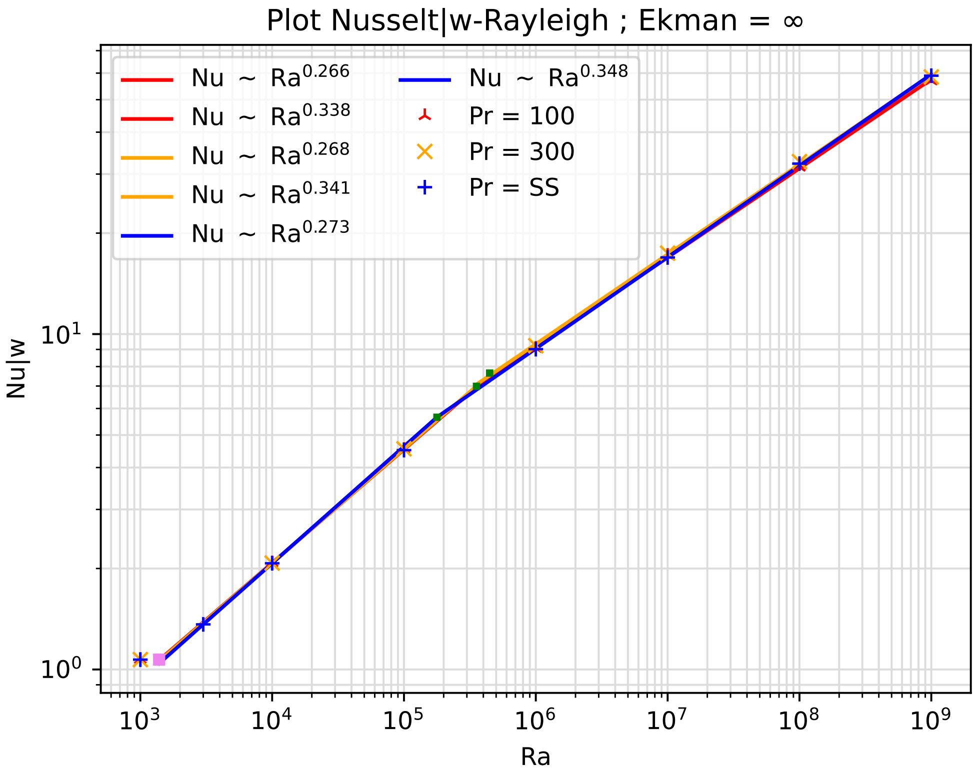

Figure 13. *Plot of the relation between parameters Rayleigh-Nusselt|Wall ; Ek* $= \infty$

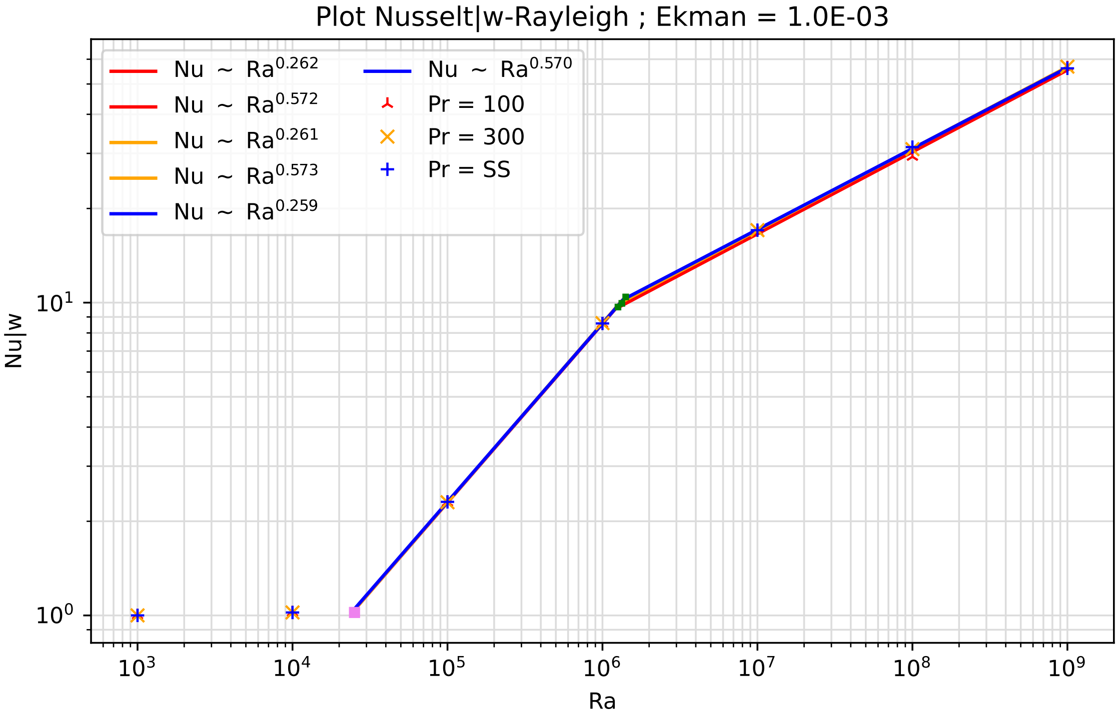

Figure 14. *Plot of the relation between parameters Rayleigh-Nusselt|Wall ; Ek* $= 1 \cdot 10^{-3}$

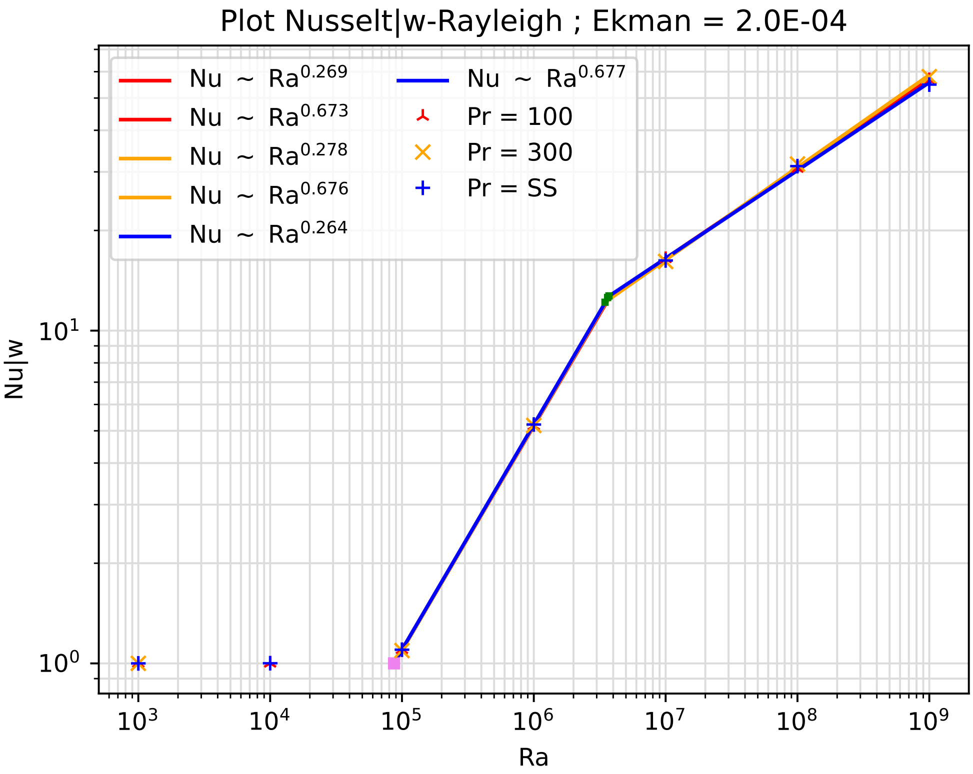

Figure 15. *Plot of the relation between parameters Rayleigh-Nusselt|Wall ; Ek* $= 2 \cdot 10^{-4}$

Kinetic_energy

Ra-Ekin

```
Ek           Pr      Regime      Slope
Infinity     100     Ramp1     1.4675
Infinity     100     Ramp2     0.7455
Infinity     300     Ramp1     1.4668
Infinity     300     Ramp2     0.7317
Infinity     SS     Ramp1     1.4632
Infinity     SS     Ramp2     0.7331
1E-03          100     Ramp1     1.9439
1E-03          100     Ramp2     0.7822
1E-03          300     Ramp1     1.9459
1E-03          300     Ramp2     0.7417
1E-03          SS     Ramp1     1.9440
1E-03          SS     Ramp2     0.7897
2E-04          100     Ramp1     2.0004
2E-04          100     Ramp2     0.7833
2E-04          300     Ramp1     1.9652
```

2E-04	300	Ramp2	0.9341
2E-04	SS	Ramp1	1.9998
2E-04	SS	Ramp2	0.8471

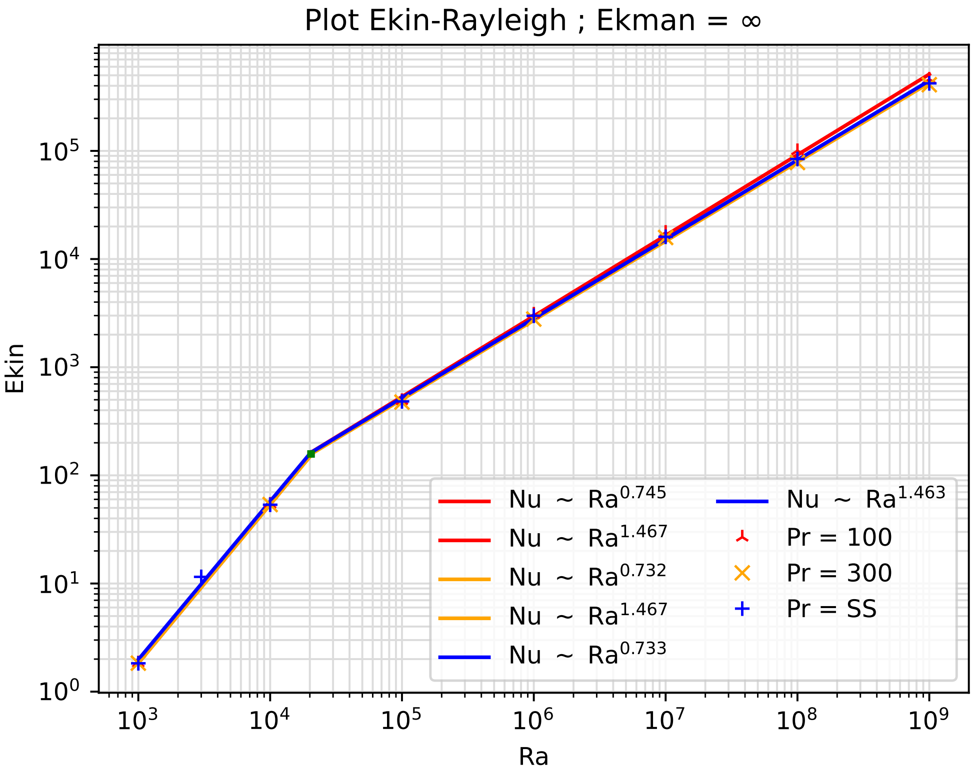

Figure 16. *Plot of the relation between parameters Rayleigh-kinetic energy; Ek* $= \infty$

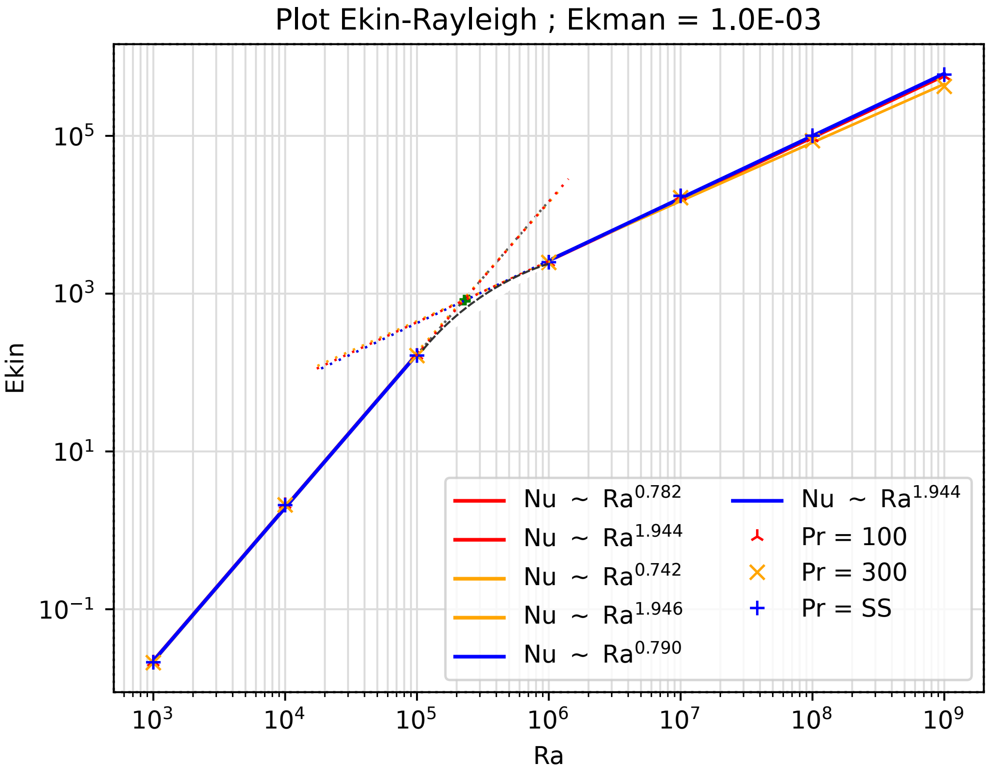

Figure 17. *Plot of the relation between parameters Rayleigh-kinetic energy ; Ek* $= 1{\cdot}10^{-3}$

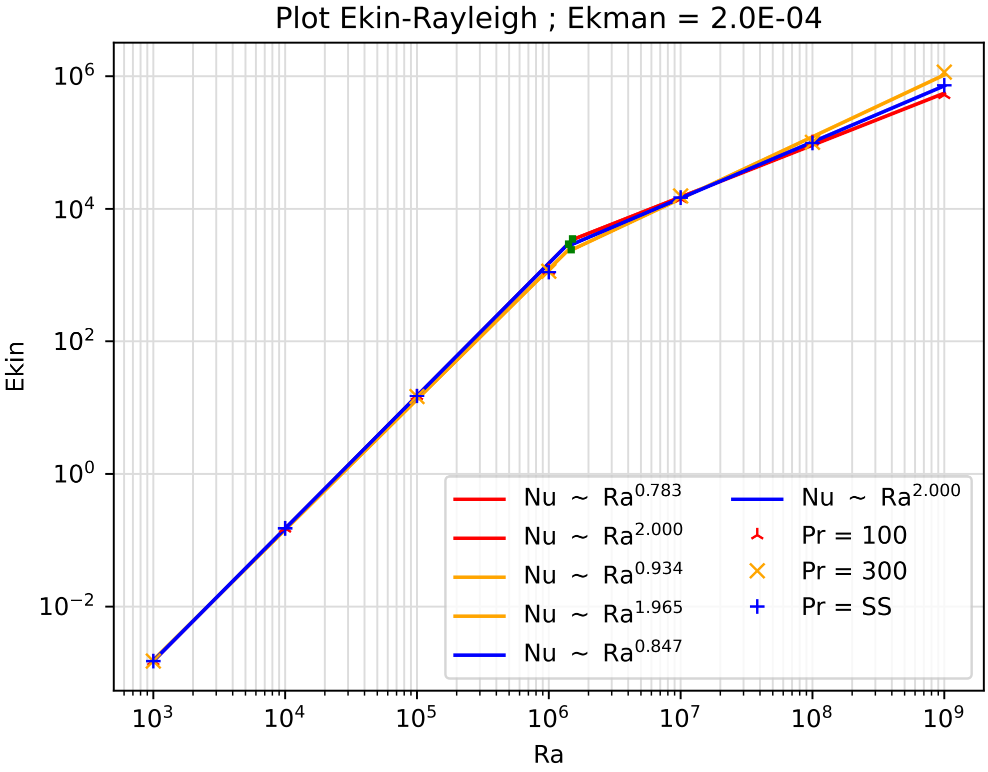

Figure 18. *Plot of the relation between parameters Rayleigh-kinetic energy ; Ek* $= 2{\cdot}10^{-4}$

4.3 Conclusions

It has been confirmed that at high Prandtl number, Nusselt and Reynolds numbers are independent of Prandtl number. This can be seen graphically from the superposition of the three curves in each plot. So we can write:

$$\mathrm{Pr} \rightarrow \infty \Rightarrow \mathrm{Nu}\,(\mathrm{Ra}\,,\mathrm{Pr}\,) = \mathrm{Nu}\,(\mathrm{Ra}\,) \tag{4.1}$$

This result is in line with the progressive reduction of the scaling exponent of Pr while increasing Pr, as shown in [Grossmann and Lohse, 2001].

In order to keep Pr constant and increase progressively Ra, we had to compute for each simulation the thermal and linear momentum diffusivities. From the Equations 3.2 is possible to deduce that the two diffusivities were decreasing linearly by the same ratio, in order to keep constant their ratio Pr and increase Ra by a quadratic function:

$$\mathrm{Ra}\; = \frac{1}{\mathrm{Pr}\,\alpha^2}$$

The scaling laws have been found for different rotative regimes, so we can start comparing the zero rotation regime ($\mathrm{Ek}\; = \infty$) with the value exposed from Grossman and Lohse and then compare the non rotating case with $\mathrm{Ek}\; = 1 \cdot 10^{-3}$ and $\mathrm{Ek}\; = 2 \cdot 10^{-4}$ cases. In [Grossmann and Lohse, 2000] is highlighted how a scaling law as a sum

$$\mathrm{Nu}\; = \alpha_1 \mathrm{Ra}^{\,1/4} + \alpha_2 \mathrm{Ra}^{\,1/3}$$

mimics the single scaling coefficient $\frac{2}{7} = 0.289$.
There are few data for large Prandtl number [Grossmann and Lohse, 2001], hence are reported the results for $\mathrm{Pr}\; < 93$ from Ashkenazi and Steinberg [Ashkenazi and Steinberg, 1999] where the scaling coefficient is found to be $\mathrm{Nu}\; \approx \mathrm{Ra}^{\,0.30 \pm 0.03}$.
In the same way, the found scaling law for $\mathrm{Pr}\; = 100$ based on two coefficients

$$\mathrm{Nu}\; = \alpha_1 \mathrm{Ra}^{\,0.340} + \alpha_2 \mathrm{Ra}^{\,0.267}$$

can mimic the result from Ashkenazi and Steinberg. This would correspond in using a single regression for the points in Figure 10.
Moreover, by comparing the Rayleigh values of the first transition in different Ekman number cases, we can deduce that rotation is causing somehow an inhibition of convective motion, thus keeping Nusselt number unitary for higher Rayleigh numbers.

Bibliography

[MPI, 1994] (1994). Mpi: A message-passing interface standard.

[Anderson et al., 1999] Anderson, Bai, and Bischof (1999). *LAPACK Users' Guide*. Society for Industrial and Applied Mathematics, Philadelphia, PA, third edition.

[Ashkenazi and Steinberg, 1999] Ashkenazi, S. and Steinberg, V. (1999). High rayleigh number turbulent convection in a gas near the gas-liquid critical point. *Physical review letters*, 83(18):3641.

[Berrut and Trefethen, 2004] Berrut, J.-P. and Trefethen, L. N. (2004). Barycentric lagrange interpolation. *SIAM Review*, 46(3):501–517.

[Busse and Whitehead, 1971] Busse and Whitehead (1971). Instabilities of convection rolls in a high prandtl number fluid. *Journal of Fluid Mechanics*, 47(2):305–320.

[Chandrasekhar, 2013] Chandrasekhar, S. (2013). *Hydrodynamic and hydromagnetic stability*. Courier Corporation.

[Davis, 1922] Davis, A. (1922). Lxxix. natural convective cooling in fluids. *The London, Edinburgh, and Dublin Philosophical Magazine and Journal of Science*, 44(263):920–940.

[Fischer et al., 2007] Fischer, Lottes, and Tufo (2007). Nek5000.

[Grossmann and Lohse, 2000] Grossmann and Lohse (2000). Scaling in thermal convection: a unifying theory. *Journal of Fluid Mechanics*, 407:27–56.

[Grossmann and Lohse, 2001] Grossmann and Lohse (2001). Thermal convection for large prandtl numbers. *Phys. Rev. Lett.*, 86:3316–3319.

[Kaminski and Jaupart, 2003] Kaminski and Jaupart (2003). Laminar starting plumes in high-prandtl-number fluids. *Journal of Fluid Mechanics*, 478:287–298.

[Munson et al., 2009] Munson, Bruce, and Young (2009). *Fundamentals of Fluid Mechanics, 6th edition*. Wiley.

[Patera, 1984] Patera, A. T. (1984). A spectral element method for fluid dynamics: Laminar flow in a channel expansion. *Journal of Computational Physics*, 54(3):468–488.

[Paul F. Fischer and Kerkemeier, 2008] Paul F. Fischer, J. W. L. and Kerkemeier, S. G. (2008). nek5000 Web page. http://nek5000.mcs.anl.gov.

[Schmitz and Tilgner, 2009] Schmitz, S. and Tilgner, A. (2009). Heat transport in rotating convection without ekman layers. *Phys. Rev. E*, 80:015305.

[Schmitz and Tilgner, 2010] Schmitz, S. and Tilgner, A. (2010). Transitions in turbulent rotating rayleigh-bénard convection. *Geophysical & Astrophysical Fluid Dynamics*, 104(5-6):481–489.

[Tritton, 2012] Tritton, D. J. (2012). *Physical fluid dynamics*. Springer Science & Business Media.

[Varé et al., 2020] Varé, T., Nouar, C., Métivier, C., and Bouteraa, M. (2020). Stability of hexagonal pattern in rayleigh–bénard convection for thermodependent shear-thinning fluids. *Journal of Fluid Mechanics*, 905.

[Verhoeven et al., 2015] Verhoeven, Wiesehöfer, and Stellmach (2015). Anelastic versus fully compressible turbulent rayleigh–bénard convection. *The Astrophysical Journal*, 805(1):62.

Appendices

Appendix 1 - Pictures and plot

Ra-Pe

```
Ek           Pr      Regime      Slope
Infinity     100     Ramp1     0.7337
Infinity     100     Ramp2     0.3727
Infinity     300     Ramp1     0.7334
Infinity     300     Ramp2     0.3659
Infinity     SS     Ramp1     0.7316
Infinity     SS     Ramp2     0.3666
1E-03          100     Ramp1     0.9719
1E-03          100     Ramp2     0.3911
1E-03          300     Ramp1     0.9730
1E-03          300     Ramp2     0.3709
1E-03          SS     Ramp1     0.9720
1E-03          SS     Ramp2     0.3949
2E-04          100     Ramp1     1.0002
2E-04          100     Ramp2     0.3916
2E-04          300     Ramp1     0.9826
2E-04          300     Ramp2     0.4671
2E-04          SS     Ramp1     0.9999
2E-04          SS     Ramp2     0.4236
```

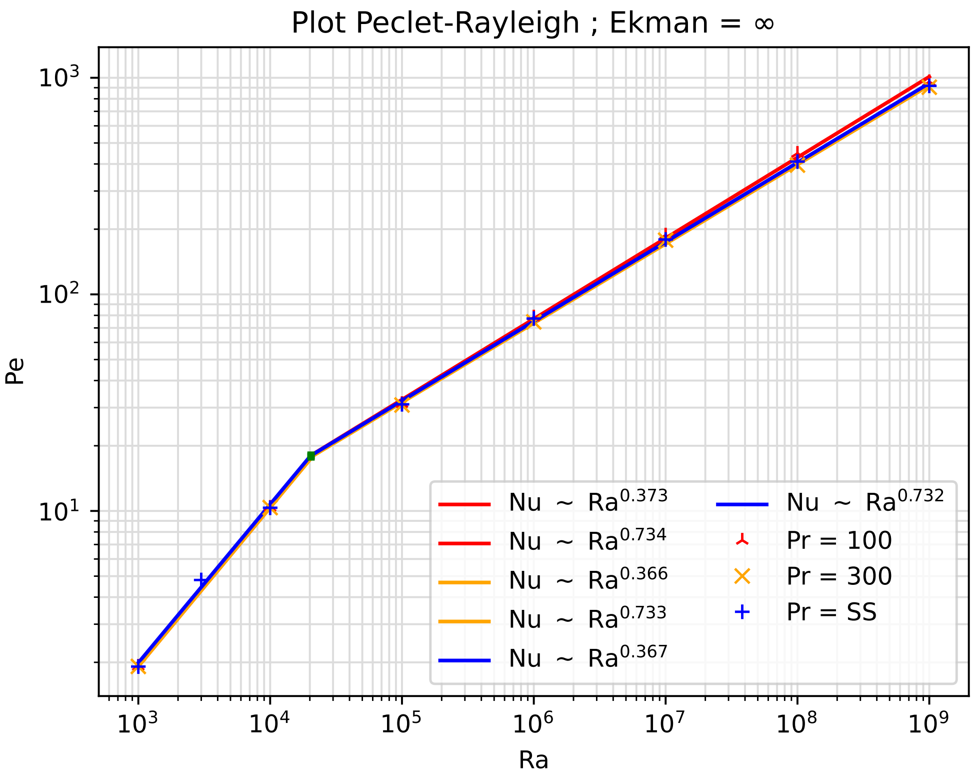

Figure 19. *Plot of the relation between parameters Rayleigh-Peclet ; Ek* $= \infty$

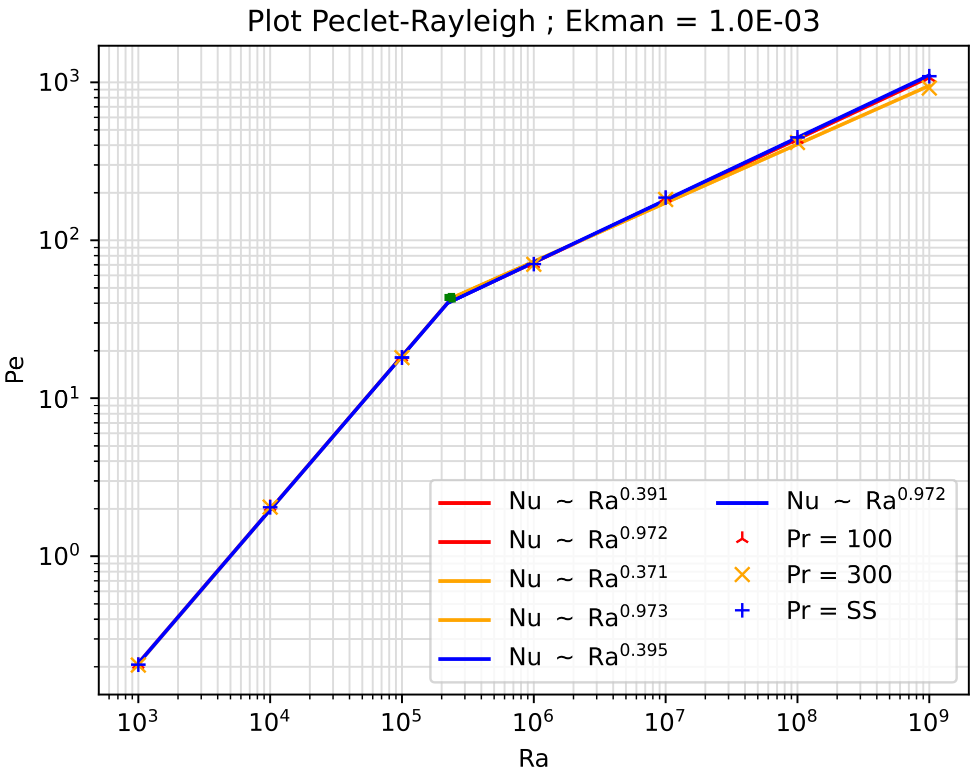

Figure 20. *Plot of the relation between parameters Rayleigh-Peclet ; Ek* $= 1 \cdot 10^{-3}$

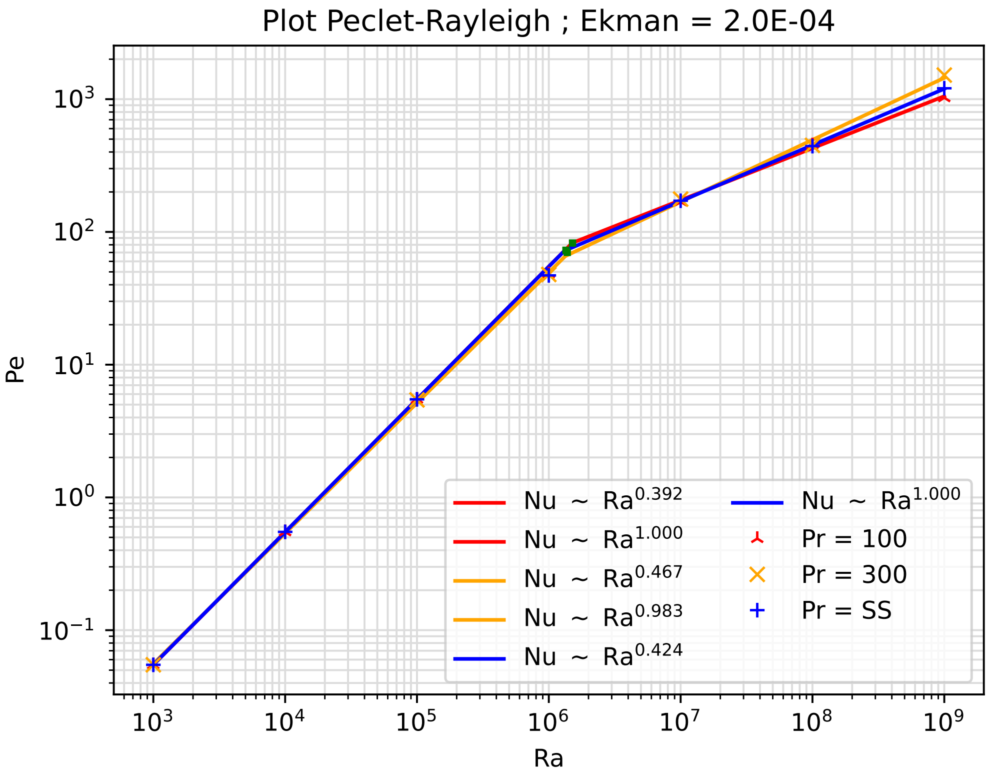

Figure 21. *Plot of the relation between parameters Rayleigh-Peclet ; Ek* $= 2 \cdot 10^{-4}$

Appendix 2 - Subroutines

```
c-----------------------------------------------------------------------
      subroutine userchk
      include 'SIZE'
      include 'TOTAL'

      real var1(nx1*ny1*nz1*nelv)



      real DTDX(lx1,ly1,lz1,lelt,ldimt)
      real DTDY(lx1,ly1,lz1,lelt,ldimt)
      real DTDZ(lx1,ly1,lz1,lelt,ldimt)

      real DvxDx(lx1,ly1,lz1,lelt,ldimt)
      real DvxDy(lx1,ly1,lz1,lelt,ldimt)
      real DvxDz(lx1,ly1,lz1,lelt,ldimt)
```

```
real DvyDx(lx1,ly1,lz1,lelt,ldimt)
real DvyDy(lx1,ly1,lz1,lelt,ldimt)
real DvyDz(lx1,ly1,lz1,lelt,ldimt)

real DvzDx(lx1,ly1,lz1,lelt,ldimt)
real DvzDy(lx1,ly1,lz1,lelt,ldimt)
real DvzDz(lx1,ly1,lz1,lelt,ldimt)

real intomegaxsq
real intomegaysq
real intomegazsq

real pol_var_x
real pol_var_y
real pol_var_z


integer i
integer e,f

real s_bar

!output for Step 0 to 100 and then every 100 Steps:
nio = -1
if (istep.le.100.or.mod(istep,100).eq.99) nio=nid

nv = nx1*ny1*nz1*nelv
nt = nx1*ny1*nz1*nelt

nxyz=lx1*ly1*lz1




if (mod(istep,100).eq.0) then
   tmax = glmax(t ,nt)
   umax = glmax(vx,nt)
   if (nid.eq.0) write(6,1) istep,time,umax,tmax
```

```
   1     format(i10,1p3e12.5,’ time,umax,tmax’)
      endif



c     global scalar
c     real function glsc3(a,b,mult,n) source
c     Input: integer n, real array a of size n, real array b of size n,
c     Returns the sum of a(i)*b(i)*mult(i), i=1..n among all processes
c     /mass/ real array bm1 of size (lx1,ly1,lz1,lelt)


c     Value of the mass of the cell (rho=1)
      var_mass = 1
c     cubic cell = 1


c     Compute total kinetic energy
      if(mod(istep,100).eq.0)then
         xke = glsc3(vx, vx, bm1, nv)
         yke = glsc3(vy, vy, bm1, nv)
         zke = glsc3(vz, vz, bm1, nv)
         total_ke = 0.5*(xke + yke + zke)/(param(8)**2*var_mass)
 if(istep.ge.1000000.and.nid.eq.0) write(6,11) "Step ", istep
         if(nid.eq.0) write(6,2) istep, time, total_ke
   2    format(i10,1p2e14.6,’  Ekin’)
  11    format(a10,i10)
      endif

c     Compute Poloidal and Toroidal (helmoltz decomposition)
      if(mod(istep,100).eq.0)then
       call gradm1(DvxDx,DvxDy,DvxDz,vx)
       call gradm1(DvyDx,DvyDy,DvyDz,vy)
       call gradm1(DvzDx,DvzDy,DvzDz,vz)
intomegaxsq= glsc3( DvzDy-DvyDz , DvzDy-DvyDz , bm1,nv)
intomegaysq= glsc3( DvxDz-DvzDx , DvxDz-DvzDx , bm1,nv)
intomegazsq= glsc3( DvyDx-DvxDy , DvyDx-DvxDy , bm1,nv)
pol_var_x=intomegaxsq/(intomegazsq+intomegaysq)
pol_var_y=intomegaysq/(intomegaxsq+intomegazsq)
```

```
pol_var_z=intomegazsq/(intomegaxsq+intomegaysq)
      endif



c     Compute Nusselt number Volume averaged with different cellsizes
c     param(8) is conductivity
      if(mod(istep,100).eq.0)then
       vol_nu1 = glsc3(vy,t,bm1,nv)
         vol_nu = 1.0+1.0/param(8)*vol_nu1/var_mass
         if(nid.eq.0) write(6,33) istep, time, vol_nu
   33    format(i10,1p2e14.6,'  Nusselt')
      endif



c   Nusselt number gradient at bottom wall:
      if(mod(istep,100).eq.0)then
       call gradm1(DTDX,DTDY,DTDZ,T)
call surf_avg(s_bar,a_surf, DTDY,2,'t  ')
!Nus_wall is negative > abs
if(nid.eq.0) write(6,36) istep, time, abs(s_bar)
   36    format(i10,1p2e14.6,'  Nuswall')
      endif



c     Compute Peclet Number
      if(mod(istep,100).eq.0)then
       v1 = glsc3(vx,vx, bm1, nv)
       v2 = glsc3(vy,vy, bm1, nv)
       v3 = glsc3(vz,vz, bm1, nv)

       v4 = (v1+v2+v3)/var_mass
       !v4 = fmdian(v3, nv, .TRUE.)
       peclet = (v4)**0.5/param(8)
         if(nid.eq.0) write(6,5) istep, time, peclet
   5    format(i10,1p2e14.6,'  Peclet')
```

```
      subroutine useric (ix,iy,iz,ieg)

C     Set initial conditions

      include 'SIZE'
      include 'TOTAL'
      include 'NEKUSE'

      ux   = RAND(I)*1e-5
      uy   = RAND(I)*1e-5
      uz   = RAND(I)*1e-5



      temp = 1.0 - y

      if(y==0) temp=1.0
      if(y==1) temp=0.0

      return
      end
```

Appendix 3 - Miscellaneous

The semi-implicit Euler method produces an approximate discrete solution by iterating the following by-step algorithm:

$$\begin{cases} v_{n+1} = v_n + g(t_n, x_n)\Delta t \\ x_{n+1} = x_n + f(t_n, v_{n+1})\Delta t \end{cases} \tag{2}$$

Where Δt is the time step. The difference with the standard Euler method is that the semi-implicit use the value v_{n+1} to compute x_{n+1}, while the standard Euler method uses v_n to compute x_{n+1}. Those are both first-order integrators, meaning that the global error is of the order of Δt.

MPI [MPI, 1994] is a communication protocol that addresses primarily the message-passing parallel programming model, in which data is moved from the address space of one process to that of another process through cooperative operations on each process. Extensions to the "classical" message-passing model are provided in collective operations, remote-memory access operations, dynamic process creation, and parallel I/O. The MPI standard include the syntax and semantics of libraries that are useful for message-passing in programs as C and Fortran. This made the open- source MPI implementations very popular in software industry.

Curl

Definition of curl (rotor): [Tritton, 2012]

$$\hat{\mathbf{n}} \cdot \nabla \times \mathbf{u} = \lim_{S \to 0} \frac{1}{S} \oint \mathbf{u} \cdot d\mathbf{l}$$

For a 3D vector field $\mathbf{F} = \big(F_x, F_y, F_z\big)$ we get:

$$\nabla \times \mathbf{F} = \begin{vmatrix} \hat{\imath} & \hat{\jmath} & \hat{k} \\ \frac{\partial}{\partial x} & \frac{\partial}{\partial y} & \frac{\partial}{\partial z} \\ F_x & F_y & F_z \end{vmatrix} = \hat{\imath}\Big(\frac{\partial F_z}{\partial y} - \frac{\partial F_y}{\partial z}\Big) + \hat{\jmath}\Big(\frac{\partial F_x}{\partial z} - \frac{\partial F_z}{\partial x}\Big) + \hat{k}\Big(\frac{\partial F_y}{\partial x} - \frac{\partial F_x}{\partial y}\Big) \quad (3)$$

Adimensionalisation

of the equation begins by defining the dimensionless counterparts of all the variables involved. We express the adimensionalisation for a generic variable φ, with subscripts r-reference and s-scale.

$$\tilde{\varphi} = \frac{\varphi - \varphi_r}{\varphi_s} \qquad \text{For example:} \qquad \tilde{x} = \frac{x - x_r}{x_s}$$

The variables to be made dimensionless will be then the components of the vectors position (u, v, w) and velocity (x, y, z), the time t and the pressure p . We can now apply some hypotheses:

- The reference value φ_r of each variable at zero
- The scaling factor is common among variables with the same dimension: the three components of the position vector (x, y, z) are scaled by the same coefficient L_s . In the same fashion, also the velocity vector components (u, v, w) share the scaling factor u_s .

This leads to the following identities:

$$\begin{cases}(x,y,z) = L_s(\tilde{x},\tilde{y},\tilde{z})\\ (u,v,w) = u_s(\tilde{u},\tilde{v},\tilde{w})\\ p = p_s\,\tilde{p}\\ t = t_s\,\tilde{t}\end{cases}$$

Also, we use the property that allow to adimensionalise also derivatives by the ratio of the involved scales, with denominator at the power of the derivation order:

$$\frac{\mathrm{d}^n\varphi}{\mathrm{d}\psi^n} = \frac{\varphi_s}{\psi_s^n}\frac{\mathrm{d}^n\tilde{\varphi}}{\mathrm{d}\tilde{\psi}^n}$$

for example, for a velocity component we have:

$$\frac{\mathrm{d}^n x}{\mathrm{d}t^n} = \frac{L_s}{t_s^n}\frac{\mathrm{d}^n\tilde{x}}{\mathrm{d}\tilde{t}^n}$$

The same property holds for partial derivatives. Hence we can apply it in the NS equation:

$$\rho\Big(\frac{u_s}{t_s}\frac{\partial\tilde{\mathbf{u}}}{\partial\tilde{t}} + (u_s\tilde{\mathbf{u}}\cdot\frac{1}{L_s}\tilde{\nabla})u_s\tilde{\mathbf{u}}\Big) = -\frac{p_s}{L_s}\tilde{\nabla}\tilde{p} + \mu\frac{u_s}{L_s^2}\tilde{\nabla}^2\tilde{\mathbf{u}} + \rho\mathbf{g}$$

We can divide by the factor $\frac{\mu u_s}{L_s^2}$ to get:

$$\frac{\rho L_s^2}{\mu t_s}\frac{\partial\tilde{\mathbf{u}}}{\partial\tilde{t}} + \underbrace{\frac{\rho u_s L_s}{\mu}}_{=\mathrm{Re}}\big(\tilde{\mathbf{u}}\cdot\tilde{\nabla}\big)\tilde{\mathbf{u}} = -\frac{p_s L_s}{\mu u_s}\tilde{\nabla}\tilde{p} + \frac{\rho\mathbf{g}L_s^2}{\mu u_s} + \tilde{\nabla}^2\tilde{\mathbf{u}} \tag{4}$$

We can see how dimensionless numbers as Reynolds comes from making the NS equation dimensionless. Additionaly, we can set the time scale t_s to be the ratio of the length scale to the velocity scale

$$t_s = \frac{L_s}{u_s}$$

and divide both sides of Equation 4 by Re number. This leads to:

$$\frac{\partial \tilde{\mathbf{u}}}{\partial \tilde{t}} + \big(\tilde{\mathbf{u}} \cdot \tilde{\nabla}\big)\tilde{\mathbf{u}} = - \underbrace{\frac{p_s}{\rho u_s^2}}_{=\mathrm{Eu}} \tilde{\nabla}\tilde{p} + \underbrace{\frac{L_s}{u_s^2}}_{=\frac{1}{\mathrm{Fr}^2}} \mathbf{g} + \frac{\mu}{\rho u_s L_s}\tilde{\nabla}^2\tilde{\mathbf{u}}$$

So we can write:

$$\frac{\partial \tilde{\mathbf{u}}}{\partial \tilde{t}} + \big(\tilde{\mathbf{u}} \cdot \tilde{\nabla}\big)\tilde{\mathbf{u}} = -\mathrm{Eu}\,\tilde{\nabla}\tilde{p} + \frac{1}{\mathrm{Fr}^2}\,\tilde{\mathbf{g}} + \frac{1}{\mathrm{Re}}\,\tilde{\nabla}^2\tilde{\mathbf{u}}$$

where $\tilde{\mathbf{g}}$ is the volume forces versor.